Mineralium Deposita
https://doi.org/10.1007/s00126-024-01262-7

ARTICLE

Magmatic evolution of the Kolumbo submarine volcano and its implication to seafloor massive sulfide formation

Simon Hector[1,2] · Clifford G. C. Patten[1,2] · Aratz Beranoaguirre[1,2] · Pierre Lanari[3] · Stephanos Kilias[4] · Paraskevi Nomikou[4] · Alexandre Peillod[1,2] · Elisabeth Eiche[1,2] · Jochen Kolb[1,2]

Received: 6 June 2023 / Accepted: 15 March 2024
© The Author(s) 2024

Abstract

Seafloor massive sulfides form in various marine hydrothermal settings, particularly within volcanic arcs, where magmatic fluids may contribute to the metal budget of the hydrothermal system. In this study, we focus on the Kolumbo volcano, a submarine volcanic edifice in the central Hellenic Volcanic Arc hosting an active hydrothermal system. Diffuse sulfate-sulfide chimneys form a Zn-Pb massive sulfide mineralization with elevated As, Ag, Au, Hg, Sb, and Tl contents. These elements have similar behavior during magmatic degassing and are common in arc-related hydrothermal systems. Trace-element data of igneous magnetite, combined with whole rock geochemistry and numerical modelling, highlights the behavior of chalcophile and siderophile elements during magmatic differentiation. We report that, despite early magmatic sulfide saturation, chalcophile element contents in the magma do not decrease until water saturation and degassing has occurred. The conservation of chalcophile elements in the magma during magmatic differentiation suggests that most of the magmatic sulfides do not fractionate. By contrast, upon degassing, As, Ag, Au, Cu, Hg, Sb, Sn, Pb, and Zn become depleted in the magma, likely partitioning into the volatile phase, either from the melt or during sulfide oxidation by volatiles. After degassing, the residual chalcophile elements in the melt are incorporated into magnetite. Trace-element data of magnetite enables identifying sulfide saturation during magmatic differentiation and discrimination between pre- and post-degassing magnetite. Our study highlights how magmatic degassing contributes to the metal budget in magmatic-hydrothermal systems that form seafloor massive sulfides and shows that igneous magnetite geochemistry is a powerful tool for tracking metal-mobilizing processes during magmatic differentiation.

Keywords Seafloor massive sulfide · Trace metal geochemistry · Magnetite · Kolumbo volcano

Introduction

The study of modern ore forming systems is crucial when trying to understand the formation of ancient mineral deposits and provides useful models for the exploration industry. In this light, actively forming seafloor massive sulfide (SMS), considered analogous to ancient polymetallic volcanogenic massive sulfide (VMS) deposits, provides important insights into understanding the formation of the latter (Halbach et al. 1989; Hannington and Scott 1989). Seafloor massive sulfide can form anywhere on the seafloor where hydrothermal activity is present (i.e., at mid-oceanic ridges, submarine arc volcanoes, rifts, hot spots, e.g., Hannington et al. 2005). Arc-related hydrothermal systems differ in many aspects from those located along mid-oceanic ridges and mature back-arc spreading centers, mostly with respect to important magmatic contributions, including metals, to

Editorial handling: F. Tornos

✉ Simon Hector
simon.hector@kit.edu

1 Institute of Applied Geosciences, Chair of Geochemistry and Economic Geology, KIT, Karlsruhe, Germany

2 Laboratory for Environmental and Raw Materials Analysis (LERA), Adenauerring 20B, 76131 Karlsruhe, Germany

3 Institute of Geological Sciences, University of Bern, 3012 Bern, Switzerland

4 Department of Geology and Geoenvironment, National and Kapodistrian University of Athens, Zografou Campus, 15784 Athens, Greece

Published online: 05 April 2024

the hydrothermal system (e.g., de Ronde et al. 2001, 2003, 2005; Hannington et al. 2005; Patten et al. 2020).

Magmatic volatile contributions to arc-related submarine hydrothermal systems like at the Kolumbo volcano (e.g., Carey et al. 2013; Kilias et al. 2013; Rizzo et al. 2016), Brothers volcano of the Kermadec arc (e.g., Berkenbosch et al. 2012; de Ronde et al. 2005, 2011; Keith et al. 2018), and SuSu Knolls in the Manus back-arc basin (e.g., Craddock et al. 2010; Thal et al. 2016; Yeats et al. 2014) show similarities with on-land porphyry-epithermal deposits (de Ronde et al. 2019). In such porphyry-epithermal deposits, metals are considered to be mostly carried by magmatic fluids exsolved from hydrous magmas in the mid- to upper crust (Richards 2011). Thus, metal fractionation by magmatic processes such as sulfide saturation and degassing appear to be key parameters for controlling the formation of metal-rich magmatic fluids in arc-related hydrothermal systems (Du and Audétat 2020; Hedenquist and Lowenstern 1994; Jenner et al. 2010). Sulfide saturation in the magma will extract most of the chalcophile and siderophile elements of a silicate magma (including As, Ag, Au, Hg, Sb, and Tl) and concentrate them into sulfide phases—e.g., immiscible sulfide liquid or crystalline sulfides—(Fontboté et al. 2017; Jenner et al. 2010; Park et al. 2015; Sun et al. 2004). Similarly, magmatic degassing leads to formation of a ligand-rich aqueous phase (e.g., Cl, S, and F) able to form complexes with metals and remove them from the magma if it is still fertile—i.e., before sulfide saturation—(Audétat 2019; Fontboté et al. 2017). If the magma reaches sulfide saturation before volatile saturation, most of the chalcophile and siderophile metals partition into sulfide phases, preventing formation of metal-rich fluids upon magmatic degassing. However, volatile bubbles may nucleate on sulfide phases to form low-buoyancy sulfide-volatile compounds, transporting sulfides—and their metals—toward the shallow part of the magmatic system (Blanks et al. 2020; Mungall et al. 2015). In addition, oxidation of the sulfides by the volatiles within the sulfide-volatile compound may lead to metal transfer to the volatile phase and eventually to the magmatic-hydrothermal system (Patten et al. 2024). Therefore, investigating the timing between sulfide and volatile saturation and degassing in the melt is crucial to understand how these processes affect the metal fertility of the magma. To do so, petrogenetic indicator minerals, such as magnetite, have proven to be useful when constraining the geochemical conditions of a magmatic-hydrothermal system (Dare et al. 2014 and references therein).

Magnetite is a common mineral in magmatic-hydrothermal system and its composition may be used to identify its origin—i.e., hydrothermal, igneous, and/or ore-deposit related—(Dare et al. 2014; Huang et al. 2019; Nadoll et al. 2014). Trace-element compositions in igneous magnetite is mainly controlled by the temperature, fO_2, and co-crystallizing phases; it provides insights into the melt composition at the time of magnetite crystallization and enables identification of simultaneous formation of other mineral phases, such as sulfides (Dare et al. 2014; Huang et al. 2019). Indeed, chalcophile elements are slightly incompatible to compatible in magnetite, and compositional variation of the melt may be recorded by the trace element content of magnetite (Dare et al. 2012).

In this study, we investigate the Kolumbo submarine volcano and its SMS in order to understand how magmatic processes contribute to the metal budget of SMS in volcanic arc magmatic-hydrothermal systems. Trace-element composition evolution of igneous magnetite and whole rock geochemistry is combined with petrology and numerical modelling to investigate the timing between sulfide saturation, volatile saturation, and degassing and to highlight how these processes affect the metal content of the magma during magmatic differentiation. This allows us to (1) estimate the metal fertility of the magma during magmatic differentiation, (2) determine the magmatic input of metals into the magmatic-hydrothermal system, and (3) ultimately derive the magmatic contributions to the formation of SMS.

Geological setting

Kolumbo volcano

The Kolumbo submarine volcano is located in the Anhydros sedimentary basin, southern Aegean Sea, as part of the Christiana-Santorini-Kolumbo volcanic field in the center of the 450-km-long Hellenic Volcanic Arc (HVA; Fig. 1 a-inset). Volcanic activity along the HVA is linked to subduction of the African Plate underneath the Aegean Microplate (Papanikolaou 2013), which can be traced back at least to the Pliocene (Fytikas et al. 1984; Preine et al. 2022). The HVA stretches from the Methana peninsula (Saronic Gulf) in the west through the islands of Milos, Antimilos, and Santorini (Cyclades) to Kos and Nisyros (Dodecanese) in the east, including submarine volcanoes (Nomikou et al. 2013; Fig. 1a-inset). Regional NW–SE extension in the west to NE–SW in the east leads to crustal thinning, exhumation of high-temperature metamorphic rocks in core complexes, and the deposition of extensional sedimentary basins (Agostini et al. 2010), including the Anhydros basin north-east of Santorini, between the islands of Ios and Anafi (Fig. 1a) (Nomikou et al. 2016). The Anhydros basin hosts the Kolumbo volcano as well as 25 other volcanic cones developed along the Christiana-Santorini-Kolumbo rift, forming the Kolumbo Volcanic Chain (Fig. 1a) (Hooft et al. 2017; Nomikou et al. 2012, 2019).

The Kolumbo volcano has been the source of seismic activity over the past few decades (e.g., earthquake swarms

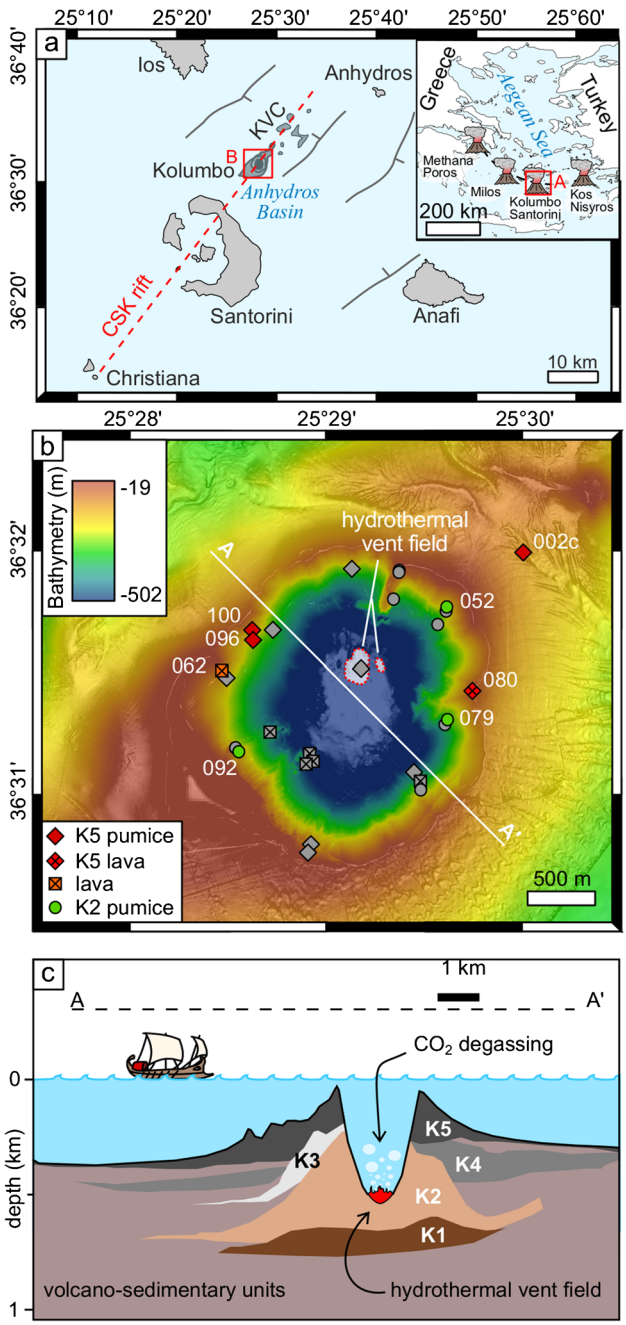

Fig. 1 Geological setting of the Kolumbo volcano. **a** Location in the Anhydros basin—CSK rift: Christiana-Santorini-Kolumbo rift; KVC: Kolumbo volcanic chain; inset: location of Kolumbo within the Hellenic Volcanic Arc. **b** Bathymetric map (modified after Nomikou et al. 2022) showing sample locations (samples from Klaver et al. 2016 in gray). **c** Schematic cross-section of the magmatic-hydrothermal system (see **b** for location), stratigraphy of the K1 to K5 volcaniclastic units based on Hübscher et al. (2015)

of 2006–2007) and is considered the most active volcanic system in the region at the present time (Dimitriadis et al. 2010). Its volcanic cone has an elongated shape oriented NE-SW with a basal diameter of 3 km. The edifice rises from 500 m below sea level (mbsl) and shoals 19 mbsl at its shallowest point (Fig. 1b; Nomikou et al. 2012). The last eruption of 1650 CE formed a 1.7 km wide crater in the center of the cone (Fouqué 1879; Sigurdsson et al. 2006). The crater slopes are steep with the crater bottom at 502 mbsl (Nomikou et al. 2012). There is a hydrothermal vent field in the northern part of the crater hosting low- to high-temperature polymetallic Zn-Pb-(As, Ag, Au, Cu, Hg, Sb, Tl)-rich sulfate-sulfide chimneys (Fig. 1b; Carey et al. 2013; Kilias et al. 2013; Nomikou et al. 2022; Rizzo et al. 2016, 2019; Sigurdsson et al. 2006). Low-temperature chimneys emit clear fluids up to 70 °C and minor gas bubbles, whereas high temperature chimneys discharge CO_2-rich fluids up to 265 °C (Nomikou et al. 2022; Sigurdsson et al. 2006). Mixing of magmatic fluid with the hydrothermal system at Kolumbo is estimated to occur at 270 °C and 1160 mbsl based on pressure and temperature geo-indicators (i.e., 650 m below the seafloor) (Rizzo et al. 2019).

Five distinct cycles of mostly submarine volcanism have been identified by seismic imaging (Hübscher et al. 2015; Preine et al. 2022). They form an assembly of five circular, cone-shaped stratigraphic units labelled K1 to K5 interbedded with volcano-sedimentary rocks (Fig. 1c) (Hübscher et al. 2015). The timing of volcanic activity is poorly constrained, but based on the stratigraphy, it is estimated to start with the second volcanic phase of the Christiana-Santorini-Kolumbo volcanic field between ca. 1.6 and 0.7 Ma (Preine et al. 2022). Only the age of the K5 unit is known and linked to the 1650 CE eruption based on witness accounts (Hübscher et al. 2015; Richard 1657).

Kolumbo was sampled in 2010 by the remotely operated vehicle (ROV) *Hercules* during the R/V *Nautilus* cruise NA007 and later by drilling during the IODP (International Ocean Discovery Program) expedition 398. At the time of writing, only in situ samples from the outcropping units K2 and K5 collected by the ROV *Hercules* were available for study. The samples were collected from basaltic to andesitic lava flows and rhyolitic pumice layers (Klaver et al. 2016). Centimeter-sized mafic enclaves in pumice typically show chilled margins, indicating injection of mafic magma into a less hot, more evolved host magma (Cantner et al. 2014; Klaver et al. 2016). Klaver et al. (2016) suggest that the Al-rich nature of Kolumbo's magma results from wherlite cumulate formation in a lower crustal reservoir from a hydrous arc magma. Rhyolitic magma is produced by prolonged differentiation of this Al-rich melt, occasionally mixing with lower crustal melts (Klaver et al. 2016). It eventually rises adiabatically to the upper magma chamber until degassing occurs. Injection of the less evolved, hydrous, mafic magma at the base of the upper chamber likely acted as an eruption trigger (Cantner et al. 2014; Klaver et al. 2016; Konstantinou 2020).

Seismic tomography and the analysis of seismic activity during the last 20 years indicates a shallow magma chamber (Chrapkiewicz et al. 2022; Dimitriadis et al. 2010; Schmid et al. 2022). Seismic tomography using data from earthquakes between 2002 and 2005 highlights a low velocity zone interpreted as a magma chamber at 6–7 km below the seafloor (Dimitriadis et al. 2010). Alternatively, Schmid et al. (2022) suggest that the strong seismic activity at these depths reflects a rheologically strong layer obstructing melt ascending toward a 2–4-km-deep magma chamber that was located by Chrapkiewicz et al. (2022) using seismic data from the PROTEUS experiment (Hooft et al. 2017). However, McVey et al. (2020), working on the same set of data, do not recognize any melts between 3 and 5 km depth. Although the exact depth and architecture of the actual uppermost magma storage at Kolumbo remains disputed, petrology- and geochemistry-based modelling by Cantner et al. (2014) estimates that rhyolitic magma was stored at a temperature of 750 °C at a depth of 5–6 km prior to the 1650 CE eruption.

Sampling and methods

Sample localities

The *Hercules* ROV allowed sampling of pumice and lava flow fragments from the K2 and K5 units, although with a sample size limit of ~ 15 cm because of limitations of the robotic arm (Fig. 1b).

Methods

Chemical analyses were performed at the Laboratory for Environmental and Raw Materials Analysis at the Institute of Applied Geosciences in Karlsruhe, Germany, with the exception of electron probe micro-analysis (EPMA), which was performed at the Institute of Geological Sciences of the University of Bern, Switzerland, and Hg content measurement by atomic absorption spectroscopy at the Oceanic and Continental Environment and Paleoenvironment mixed research unit (UMR EPOC) in Bordeaux, France. Petrography was done via transmitted and reflected light microscopy.

Whole rock geochemistry

Major element compositions of whole rocks ($n = 13$) were measured by X-ray fluorescence (XRF; S4 Explorer, Bruker AXS) on glass beads with BHVO-1, MRG-1, RGM-1, and SY-2 as reference materials, as a measure of analytical precision and accuracy (Table 1, ESM 1). Carbon and sulfur contents were measured on rock powder by solid state infrared absorption using a Carbon–Sulfur Analyzer (CS-2000, Eltra) with steel (92,400–3050), ductile iron (92,400–3100), and barium sulfate (90,821) standards from Eltra as reference material as a measure of analytical precision and accuracy (see ESM 1). Trace element contents ($n = 13$, Table 2) were measured by laser ablation-inductively coupled plasma-mass spectrometry (LA-ICP-MS) on pressed powder pellets using a Teledyne 193 nm Excimer Laser coupled to an ICP-MS (Element XR ThermoFisher) with spot size of 85 µm; laser frequency of 10 Hz, fluence of 5 J·cm^{-2}; and He, Ar, and N flow of 0.3 L·min^{-1}, 0.85 L·min^{-1}, and 10 mL·min^{-1}, respectively. Pressed powder pellets were prepared following the method described in Patten et al. (2023). Calibration and data quality were checked using pressed powder pellets of standards BHVO-1, BHVO-2, BCR-2, and BIR-1 from the USGS. In order to improve data quality, Au contents were measured a second time, on the same equipment, following the method of ultra-low detection of Au on pressed powder pellets by LA-ICP-MS developed by Patten et al. (2023). Calibration and data quality were checked using pressed power pellets of standards BHVO-2, BCR-2, and BIR-1 from the USGS, MRG-1, and TDB-1 from NRCan and TSD-41, an in-house epidosite standard. Data reduction of all LA-ICP-MS analysis was done using the Iolite software 3DRS plugin v.4.8.3 (Paton et al. 2011). Accuracy and precision for reference materials (< 15% for most elements) as well as limits of detections are detailed in Supplementary data (see ESM 1). The Hg content was measured by spectrophotometry with a direct Hg analyzer DMA-80 (Milestone) using standards BCR-277R and TCEGir (in-house) for calibration (see ESM 1).

Magnetite composition

The major element compositions of magnetite ($n = 77$ from 7 samples, Table 3) were measured by EPMA (JEOL JXA-8200 Superprobe) using the following synthetic and natural standard reference materials: anorthite (Al_2O_3, CaO), orthoclase (SiO_2), magnetite (FeO), forsterite (MgO), rutile (TiO_2), metal nickel (NiO), spinel (Cr_2O_3), sphalerite (ZnO), and pyrolusite (MnO). Spot analyses for Al, Si, Ca, Fe, Mg, Ti, Ni, Cr, Zn, and Mn were performed using 15 keV accelerating voltage, 20 nA specimen current, and 40 s dwell time (10 s for each background after 20 s on a peak) (see ESM 2). The trace element compositions of magnetite ($n = 143$ from 8 samples, Table 4) were measured by in situ LA-ICP-MS analysis, on the same equipment as for the pellet LA-ICP-MS analyses, with spot size of 35 µm, laser frequency of 10 Hz, fluence of 5 J.cm^{-2}, and He and N flow of 0.3 L·min^{-1} and 10 mL·min^{-1}, respectively. Iron data from the EMPA was used for internal standard calibration of the LA-ICP-MS data. Calibration and data quality was checked using Fe-rich basaltic glasses BHVO-2, BCR-2, and BIR-1 from the USGS, following the method from Dare et al.

Table 1 Major element compositions of samples from Kolumbo determined by XRF analysis (see ESM 1 for detailed data, location coordinates for each sample, and data for standards used)

Sample	Details	Lithology	SiO_2 (wt%)	TiO_2 (wt%)	Al_2O_3 (wt%)	Fe_2O_3tot (wt%)	MnO (wt%)	MgO (wt%)	CaO (wt%)	Na_2O (wt%)	K_2O (wt%)	P_2O_5 (wt%)	LOI (wt%)	Sum (wt%)
NA007-100b (enclave)	Pumice (K5)	Basaltic andesite	53.01	0.75	16.28	7.61	0.14	4.56	8.82	3.06	1.24	0.15	2.97	98.57
NA007-100c (enclave)	Pumice (K5)	Basaltic andesite	55.73	0.65	15.63	6.61	0.13	3.87	7.68	3.22	1.51	0.14	4.14	99.30
NA007-080c2	Lava (K5)	Basaltic andesite	54.78	0.79	17.72	6.32	0.10	3.69	8.17	3.02	1.52	0.15	2.60	98.85
NA007-062c	Lava (K5)	Andesite	59.03	0.76	16.29	5.98	0.13	2.27	5.64	3.54	1.89	0.18	3.45	99.15
NA007-080c3	Lava (K5)	Andesite	59.04	0.76	16.41	6.48	0.14	2.24	5.72	3.62	1.85	0.18	2.67	99.10
NA007-002c	Pumice (K5)	Trachyte	64.03	0.35	12.61	2.83	0.07	0.80	2.13	5.69	2.94	0.07	7.07	98.62
NA007-100b (matrix)	Pumice (K5)	Rhyolite	70.24	0.11	12.59	1.70	0.08	0.37	1.22	4.31	3.71	0.03	4.83	99.19
NA007-100c (matrix)	Pumice (K5)	Rhyolite	70.71	0.11	12.51	1.75	0.08	0.31	1.17	4.19	3.74	0.03	4.51	99.12
NA007-079c	Pumice (K2)	Rhyolite	70.00	0.11	12.46	1.75	0.08	0.30	1.12	4.33	3.68	0.03	5.99	99.85
NA007-096c	Pumices (K5)	Rhyolite	69.87	0.08	12.02	1.38	0.09	0.21	0.80	4.77	3.69	0.02	5.88	98.80
NA007-052c	Pumice (K2)	Rhyolite	70.74	0.09	12.45	1.49	0.09	0.19	0.90	4.45	3.66	0.03	5.02	99.11
NA007-092c	Pumice (K2)	Rhyolite	71.80	0.09	12.63	1.54	0.09	0.14	0.90	4.34	3.61	0.03	4.32	99.50
NA007-080c1	Lava (K5)	Rhyolite	72.77	0.10	12.98	1.59	0.09	0.14	0.97	4.46	3.76	0.03	2.84	99.70

(2012). Data reduction was done using the Iolite software 3DRS plugin. Accuracy and precision for reference materials (< 15% for most elements) as well as limits of detections are detailed in the Supplementary data (see ESM 2).

Results

Petrography

Samples recovered from the Kolumbo volcano come from the K2 and K5 volcanic units ($n = 3$ and $n = 10$, respectively). Two types of samples were collected: intermediate to felsic pumice (K2 and K5 units) and mafic to felsic lava (K5 unit only; Fig. 2a–d). As the samples are mostly composed of a glass to microcrystalline matrix, their igneous classification cannot be determined petrographically. Further distinctions (e.g., rhyolite pumice vs. trachyte pumice) are based on geochemical data described below.

K2 unit

The K2 unit consists of a thick (10 s of m) volcaniclastic sequence overlain by younger volcano-sedimentary units and locally outcrops on the slopes of the crater (Hübscher et al. 2015). The samples are light gray pumice with ~ 40 vol.% vesicles (< 1 mm), locally with dark gray bands (Fig. 2d). The glass matrix contains 1 to 3 vol.% phenocrysts, mostly plagioclase, biotite, and magnetite (< 1 vol.%) as well as rare orthopyroxene, amphibole, and quartz. Mafic microcrystalline enclaves are ubiquitous (~ 1 vol.%) and range from < 1 mm to 2 cm in size (Fig. 2c, d). They are composed of 30 to 50 vol.% microcrystalline matrix with acicular plagioclase, amphibole and magnetite (< 1 vol.%) containing larger phenocrysts of amphibole, clinopyroxene, and plagioclase (< 500 µm). The enclaves have a quenched texture on their margin where the contact with the matrix is sharp, indicative of rapid crystallization (Fig. 2c). The contact usually displays increased vesicularity when compared to the rest of the rock.

K5 unit

The K5 unit consists of a 10 s-of-m thick volcaniclastic sequence, with lava flows shaping Kolumbo's volcanic cone since the 1650 CE eruption (Hübscher et al. 2015; Klaver et al. 2016). The K5 pumice is white to gray with 40 to 70 vol.% vesicles and contains 1 to 3 vol.% phenocrysts: mostly plagioclase, biotite, and magnetite (< 1 vol.%) as well as rare apatite, orthopyroxene, amphibole, and quartz (Fig. 2b). The

Table 2 Trace element composition of samples from Kolumbo determined by LA-ICP-MS analysis, except where indicated (see ESM 1 for detailed data, location coordinates for each sample, and data for standards used)

Sample	Sc (µg·g^{-1})	Ti (µg·g^{-1})	V (µg·g^{-1})	Co (µg·g^{-1})	Ni (µg·g^{-1})	Cu (µg·g^{-1})	Zn (µg·g^{-1})	As (µg·g^{-1})	Mo (µg·g^{-1})	Sn (µg·g^{-1})	Hg (µg·g^{-1})*	Pb (µg·g^{-1})	Ag (ng·g^{-1})	Sb (ng·g^{-1})	Te (ng·g^{-1})	Au (ng·g^{-1})**	Tl (ng·g^{-1})	Bi (ng·g^{-1})
NA007-100b (enclave)	2.5 ± 0.2	444 ± 162	8.4 ± 1.2	2.15 ± 0.27	1.5 ± 0.9	7.7 ± 0.5	32.1 ± 3.3	1.18 ± 0.03	4.0 ± 0.1	2.0 ± 0.1	23.01	11.2 ± 0.2	63 ± 7	116 ± 6	28 ± 7	0.26 ± 0.1	419 ± 16	82 ± 6
NA007-100c (enclave)	2.0 ± 0.1	371 ± 36	7.5 ± 0.7	1.84 ± 0.12	0.6 ± 0.1	6.6 ± 0.3	25.9 ± 2.5	0.96 ± 0.02	3.0 ± 0.1	1.6 ± 0.1	n.d	9.5 ± 0.4	53 ± 7	93 ± 5	14 ± 9	0.21 ± 0.21	355 ± 13	68 ± 3
NA007-080c2	12.7 ± 1.2	3025 ± 319	133.2 ± 10.9	12.54 ± 1.09	7.8 ± 0.9	52.9 ± 4.4	32.1 ± 5.6	0.35 ± 0.02	0.4 ± 0.3	3.1 ± 0.6	24.41	4.2 ± 0.3	41 ± 5	45 ± 3	n.d	1.02 ± 0.33	58 ± 7	8 ± 2
NA007-062c	13.7 ± 0.4	4335 ± 217	108.0 ± 8.6	11.72 ± 0.42	0.9 ± 0.1	19.5 ± 0.5	73.0 ± 6.2	0.77 ± 0.03	2.4 ± 0.1	2.0 ± 0.1	23.70	9.1 ± 0.4	71 ± 5	77 ± 4	11 ± 2	0.88 ± 0.08	152 ± 11	33 ± 3
NA007-080c3	13.6 ± 0.7	4224 ± 110	108.1 ± 5.4	12.61 ± 0.53	0.9 ± 0.1	16.0 ± 0.9	67.7 ± 3.7	0.56 ± 0.03	2.0 ± 0.2	1.2 ± 0.2	23.21	8.4 ± 0.2	73 ± 5	53 ± 6	9 ± 7	0.68 ± 0.16	138 ± 5	24 ± 1
NA007-002c	7.9 ± 0.3	2075 ± 146	20.4 ± 0.8	4.50 ± 0.10	1.1 ± 0.3	25.8 ± 1.2	37.4 ± 2.1	1.97 ± 0.05	3.5 ± 0.2	3.1 ± 0.1	26.51	14.5 ± 0.2	110 ± 4	260 ± 19	24 ± 4	0.67 ± 0.21	335 ± 7	45 ± 3
NA007-100b (matrix)	22.3 ± 0.8	4238 ± 113	185.2 ± 3.8	25.21 ± 0.51	14.1 ± 1.1	29.8 ± 2.6	53.8 ± 3.5	0.89 ± 0.03	1.4 ± 0.1	1.2 ± 0.1	23.91	5.0 ± 0.2	61 ± 5	75 ± 10	5 ± 5	0.03 ± 0.54	159 ± 21	29 ± 4
NA007-100c (matrix)	18.0 ± 1.2	3419 ± 250	147.5 ± 12.3	19.06 ± 0.95	11.3 ± 0.6	22.8 ± 2.1	51.1 ± 6.1	0.95 ± 0.05	1.5 ± 0.2	1.3 ± 0.1	24.98	6.2 ± 0.5	71 ± 10	75 ± 4	8 ± 3	0.00 ± 0.26	194 ± 14	41 ± 5
NA007-079c	2.7 ± 1.2	567 ± 33	10.5 ± 0.8	3.56 ± 0.34	0.6 ± 0.1	12.0 ± 1.6	40.6 ± 2.3	1.40 ± 0.05	4.1 ± 0.2	2.3 ± 0.1	25.58	11.5 ± 0.8	118 ± 145	192 ± 9	23 ± 8	0.53 ± 0.17	437 ± 19	91 ± 9
NA007-096c	1.6 ± 0.1	244 ± 11	0.7 ± 0.1	0.63 ± 0.05	0.2 ± 0.1	15.2 ± 9.1	37.9 ± 2	1.39 ± 0.19	4.2 ± 0.4	2.5 ± 0.1	23.73	13.2 ± 1.9	174 ± 188	204 ± 40	22 ± 6	0.04 ± 0.14	451 ± 31	93 ± 4
NA007-052c	1.4 ± 0.1	359 ± 24	1.9 ± 0.1	2.36 ± 0.08	0.2 ± 0.1	20.5 ± 0.7	33.2 ± 1.9	1.20 ± 0.02	3.7 ± 0.1	3.5 ± 0.2	22.44	11.4 ± 0.3	113 ± 12	136 ± 4	24 ± 7	0.29 ± 0.08	415 ± 18	86 ± 9
NA007-092c	1.5 ± 0.1	294 ± 56	1.0 ± 0.5	3.20 ± 0.77	0.3 ± 0.2	31.5 ± 6.5	33.1 ± 2.2	1.25 ± 0.13	3.6 ± 0.3	5.4 ± 1.0	26.32	11.1 ± 0.4	184 ± 21	158 ± 33	17 ± 7	0.04 ± 0.05	416 ± 18	76 ± 6
NA007-080c1	1.3 ± 0.1	439 ± 40	2.8 ± 0.1	1.24 ± 0.10	0.2 ± 0.1	8.6 ± 0.7	33.3 ± 3.8	1.12 ± 0.03	3.5 ± 0.3	2.2 ± 0.1	23.92	10.4 ± 0.6	54 ± 6	132 ± 12	n.d	0.21 ± 0.16	441 ± 23	35 ± 2

*Spectrophotometry data; **ultra-low detection of Au LA-ICP-MS data (see Methods). Abbreviation: *n.d.*, non-determined

K5 lava usually contains < 5 vol.% vesicles, 60 vol.% microcrystalline matrix, and 35 vol.% phenocrysts (Fig. 2a). The phenocrysts are clinopyroxene, plagioclase, amphibole, and magnetite (< 1 vol.%). In both pumice and lava, phenocrysts occur locally as single plagioclase or amphibole grains (< 2 cm) showing evidence of resorption, or as agglomerate (< 2 mm) containing plagioclase ± amphibole ± clinopyroxene ± magnetite and < 50 vol.% vesicles (Fig. 2a, b, g, h). Mafic microcrystalline enclaves are ubiquitous (~ 1 vol.%) and are similar to those in K2. They range from < 1 mm to 2 cm in size and have a quenched margin, again suggestive of rapid crystallization. They are composed of 30 to 50 vol.% microcrystalline matrix with acicular plagioclase, amphibole, and magnetite (< 1 vol.%) containing larger phenocrysts of amphibole, clinopyroxene, and plagioclase (< 500 µm). The contact with the host rock is sharp and shows increased vesicularity (Fig. 2e).

Magnetite

Magnetite is ubiquitous within the volcanic samples of Kolumbo and shows three main habits: (1) small (< 50 µm), idiomorphic magnetite in enclaves where it is disseminated in the matrix and forms inclusions in silicates or is locally associated with sulfides (Fig. 2e); (2) sub-idiomorphic to idiomorphic magnetite (< 100 µm) in the matrix, where it is usually fractured or fragmented and locally contains sulfide inclusions (Fig. 2f); and (3) sub-idiomorphic magnetite (< 200 µm) in clusters, where it is usually fractured and rounded, locally has sulfide inclusions, and may show compositional zoning (Fig. 2f, g).

Sulfides

Sulfides, although relatively scarce, are present in most of the volcanic samples of Kolumbo. The most common mineral is pyrrhotite along with lesser chalcopyrite and pyrite (Fig. 2e, f, i–k). They form xenomorphic grains that are usually < 100 µm, but can be at the mm-scale (Fig. 2j, k). The grains are usually monomineralic (i.e., pyrrhotite or chalcopyrite) but may form a pyrrhotite-chalcopyrite-pyrite assemblage, locally replaced by magnetite and goethite (Fig. 2i). In addition, sulfides locally occur as inclusions (< 10 µm) in all types of magnetite and in the phenocrysts (Fig. 2f, h).

Geochemistry

Whole rock geochemistry of pumice, lava, and enclave samples

Major element compositions of pumice, lava, and enclave samples indicate a lithological diversity ranging from

Table 3 Major element compositions of magnetite (see ESM 2 for detailed data). Note that the data are sorted by increasing MgO content in the host-rock

	NA007-092c	NA007-079c	NA007-100c (matrix)	NA007-002c	NA007-062c	NA007-080c2	NA007-100c (enclave)
MgO (wt%) host-rock	0.14	0.30	0.31	0.80	2.27	3.69	3.87
(wt%)	$n=10$	$n=7$	$n=10$	$n=14$	$n=11$	$n=10$	$n=14$
SiO_2	1.72 ± 5.03	0.20 ± 0.15	0.74 ± 1.62	0.08 ± 0.02	0.15 ± 0.11	0.09 ± 0.03	6.60 ± 20.27
TiO_2	10.21 ± 1.15	10.10 ± 4.95	4.93 ± 2.15	12.66 ± 0.19	12.11 ± 0.47	10.55 ± 1.52	6.48 ± 2.15
Al_2O_3	3.95 ± 0.74	1.64 ± 0.46	1.51 ± 0.37	1.90 ± 0.06	1.50 ± 0.05	3.65 ± 1.21	2.27 ± 2.32
FeO	76.35 ± 7	81.29 ± 3.18	84.37 ± 1.73	78.66 ± 0.59	79.83 ± 0.57	77.03 ± 1.14	75.66 ± 21.6
MnO	0.54 ± 0.08	1.27 ± 0.3	1.60 ± 0.34	0.66 ± 0.01	1.41 ± 0.07	0.41 ± 0.05	1.23 ± 0.39
MgO	3.15 ± 2.19	0.45 ± 0.11	0.73 ± 0.11	1.42 ± 0.05	0.39 ± 0.04	2.72 ± 1.19	0.97 ± 0.33
CaO	0.41 ± 1.15	0.04 ± 0.03	0.06 ± 0.04	0.06 ± 0.03	0.04 ± 0.02	0.07 ± 0.09	0.27 ± 0.26
Cr_2O_3	0.05 ± 0.01	0.02 ± 0.01	0.01 ± 0.01	0.04 ± 0.01	0.01 ± 0.01	0.64 ± 1	0.03 ± 0.01
NiO	0.02 ± 0.01	0.01 ± 0	0.02 ± 0.01	0.01 ± 0.01	0.01 ± 0	0.06 ± 0.03	0.01 ± 0.01
ZnO	0.08 ± 0.05	0.18 ± 0.05	0.16 ± 0.05	0.09 ± 0.03	0.18 ± 0.04	0.09 ± 0.05	0.13 ± 0.05
Total	96.46 ± 1.54	95.18 ± 1.68	94.10 ± 0.75	95.57 ± 0.61	95.63 ± 0.47	95.29 ± 1.77	93.63 ± 1.58

Table 4 Trace elements composition of magnetite (see ESM 2 for detailed data). Note that the data are sorted by increasing MgO content in the host-rock

Sample	NA007-080c1	NA007-092c	NA007-079c	NA007-100b (matrix)	NA007-002c	NA007-080c3	NA007-062c	NA007-080c2
MgO (wt%) host-rock	0.14	0.14	0.30	0.37	0.80	2.24	3.54	3.69
($\mu g \cdot g^{-1}$)	$n=21$	$n=10$	$n=3$	$n=10$	$n=14$	$n=45$	$n=18$	$n=22$
P	1817 ± 6266	< LOD	165 ± 185	783 ± 2459	< LOD	< LOD	< LOD	192 ± 190
Sc	15 ± 10	2.54 ± 2.23	23 ± 14	4.22 ± 0.51	24.82 ± 1.31	26 ± 8	20 ± 10	26 ± 2
V	547 ± 107	490 ± 90	627 ± 78	442 ± 35	2152 ± 73	3824 ± 484	2911 ± 1684	5876 ± 227
Cr	25 ± 12	33 ± 24	22 ± 14	21 ± 8	15 ± 6	46 ± 83	58 ± 54	338 ± 100
Mn	9969 ± 1096	8854 ± 3160	10,682 ± 574	11,870 ± 1284	4476 ± 209	3629 ± 715	5962 ± 2895	3743 ± 316
Co	23 ± 5	40 ± 15	32 ± 10	31 ± 8	87.51 ± 2.74	167 ± 26	146 ± 87	251 ± 14
Ni	5.01 ± 1.74	7.05 ± 2.07	6.76 ± 1.67	3.42 ± 1.50	9.8 ± 0.41	13 ± 4	12 ± 6	221 ± 37
Cu	33 ± 37	24 ± 22	20 ± 15	4.26 ± 3.36	10.3 ± 3.3	11 ± 7	23 ± 23	140 ± 61
Zn	2694 ± 1562	2475 ± 1432	3589 ± 2070	1150 ± 136	634.44 ± 54.7	520 ± 93	1100 ± 886	947 ± 88
Ga	13 ± 2	18 ± 17	11 ± 1	15 ± 1	13.66 ± 1.03	15 ± 2	17 ± 4	15 ± 1
Ge	21 ± 20	18 ± 18	36 ± 28	4.08 ± 0.64	0.25 ± 0.37	< LOD	4.50 ± 9.73	5.97 ± 1.02
As	34 ± 36	74 ± 83	60 ± 51	1.42 ± 1.03	0.11 ± 0.23	1.31 ± 1.11	6.77 ± 17.76	3.82 ± 1.94
Y	73 ± 99	5.21 ± 8.31	82 ± 71	0.79 ± 0.57	0.27 ± 0.24	0.07 ± 0.32	4.46 ± 21.10	2.07 ± 1.05
Zr	200 ± 188	52 ± 40	1935 ± 2838	17 ± 3	42.86 ± 3.95	53 ± 24	58 ± 63	56 ± 8
Nb	164 ± 84	103 ± 20	235 ± 123	114 ± 16	13.35 ± 3.91	9.52 ± 5.41	48 ± 65	8.43 ± 1.33
Mo	39 ± 8	34 ± 2	45 ± 9	56 ± 8	4.14 ± 0.23	1.62 ± 1.07	16 ± 21	3.51 ± 0.83
Ag	0.12 ± 0.12	< LOD	0.3 ± 0.29	0.02 ± 0.02	< LOD	< LOD	0.02 ± 0.06	0.01 ± 0.04
Sn	3.78 ± 2.33	4.18 ± 3.27	4.63 ± 1.09	3.06 ± 1.53	3.23 ± 0.19	1.74 ± 1.41	2.29 ± 2.02	4.59 ± 0.54
Sb	3.11 ± 3.4	17 ± 17	6.35 ± 5.52	< LOD	< LOD	< LOD	0.34 ± 1.13	1.5 ± 0.53
Hf	3.19 ± 2.89	< LOD	36.37 ± 54.65	< LOD	< LOD	1.43 ± 0.68	1.16 ± 0.85	1.57 ± 0.24
Ta	3.53 ± 0.82	3.05 ± 1.23	4.09 ± 0.97	4.09 ± 0.49	0.72 ± 0.26	0.42 ± 0.26	1.43 ± 1.59	0.38 ± 0.07
W	3.22 ± 3.7	0.16 ± 0.25	6.37 ± 5.57	< LOD	< LOD	< LOD	0.28 ± 1.31	0.08 ± 0.13
Pb	41 ± 65	727 ± 726	94 ± 83	0.85 ± 1.48	0.16 ± 0.58	2.46 ± 2.87	1.62 ± 4.85	23 ± 18
Bi	0.02 ± 0.02	0.41 ± 0.59	0.06 ± 0.05	< LOD	< LOD	< LOD	< LOD	0.03 ± 0.03

basaltic andesite to rhyolite where the trace element content varies as the MgO content decreases (Table 1 and 2). If MgO > 0.9 wt%, Ag, As, Hg, Pb, Sb, Sn, and Tl contents increase, whereas Au, Co, Cu, Fe, Ni, Ti, V, and Zn contents remain relatively constant. In samples with MgO < 0.9 wt%, Ag, As, Au, Co, Cu, Hg, Pb, Sb, Sn, and Zn contents decrease, and Bi and Tl contents increase (Table 1 and 2).

Magnetite geochemistry

Magnetite shows limited major element variation in all samples (Table 3). The Al, Co, Cr, Cu, Ga, Mg, Ni, Sc, and V contents are higher in magnetite hosted in more mafic samples than in those hosted in felsic samples. Conversely, the Ag, As, Bi, Ge, Hf, Mn, Mo, Nb, P, Pb, Sb, Sn, Ta, Ti, W, Y, Zn, and Zr contents are higher in magnetite from felsic samples than in those in more mafic samples (Table 4).

Melt evolution modelling with COMAGMAT 3.75

The evolution of the melt was modelled using COMAGMAT 3.75 (Ariskin and Barmina 2004) to decipher the processes leading to metal mobilization from the melt. This model is based on a combination of empirical and thermodynamic calculations of mineral-melt equilibrium and can simulate magma fractionation. An average whole rock composition of the three most mafic sample compositions was used as a proxy for the starting composition of the melt and the accuracy of the model is controlled by geochemical data. However, because there was a limited number of available samples, the model is not very well constrained between 0.8–2.0 and 2.5–3.0 wt% MgO. The pressure constraints were set to decrease from 200 to 90 MPa to reflect the ascending melt in an upper reservoir located between 6 and 3 km depth. Multiple runs of the model using various redox conditions (fO_2 FMQ + 0.5 to 1.5) and variable H_2O content (1 to 3 wt%) show that the starting conditions producing a model best fitting the evolution of the major element compositions are fO_2 FMQ + 1 and 2.0 wt% H_2O (Fig. 3). Using these best fit parameters, the model suggests that magnetite crystallization starts as

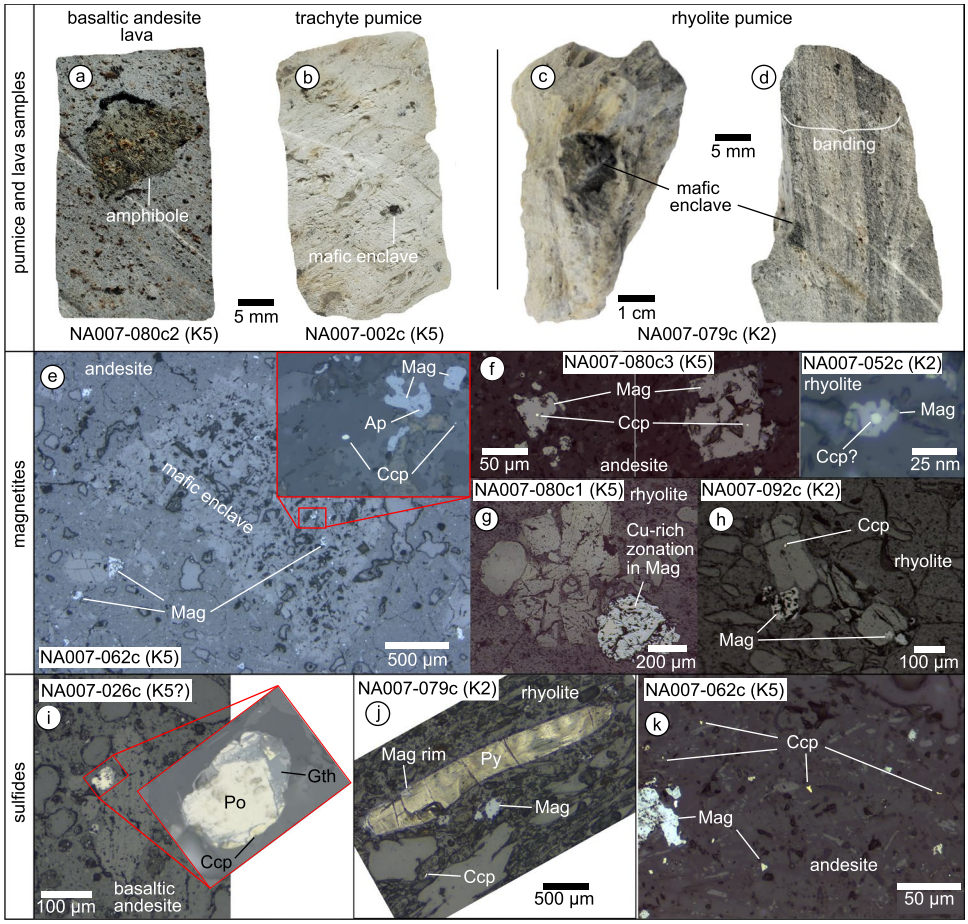

Fig. 2 Petrography of volcanic rocks. **a** Basaltic andesite lava sample with an amphibole xenocryst. **b** Trachyte pumice with mafic enclave. **c**, **d** Rhyolite pumice with banded texture and mafic enclaves with chilled margin. **e** Mafic enclave with disseminated magnetite and sulfides in andesite matrix with disseminated magnetite. **f** Idiomorphic magnetite with sulfide inclusions. **g**, **h** Phenocryst clusters with plagioclase, amphibole and magnetite, locally containing sulfide inclusions. **i** Sulfide bleb of pyrrhotite and chalcopyrite with oxidized goethite rim in basaltic andesite pumice. **j** Pyrite with magnetite rim in rhyolite pumice with chalcopyrite and magnetite. **k** Disseminated chalcopyrite and magnetite in andesite matrix. Abbreviations: Ap, apatite; Ccp, chalcopyrite; Gth, goethite; Mag, magnetite; Po, pyrrhotite; Py, pyrite

the melt reaches 2.5 wt% MgO, whereas the petrography shows an earlier occurrence of magnetite. This discrepancy is addressed in the following discussion. In addition, the water content increases during magmatic differentiation from 2.0 to 4.3 wt% H_2O at 0.9 wt% MgO, whereupon water saturation is reached and the water content decreases to 2.9 wt% in the most evolved melt.

Discussion

Magmatic differentiation at Kolumbo

Major element compositions of our samples together with data from previous studies (Cantner et al. 2014; Klaver et al. 2016) show that the K2 and K5 units record similar differentiation processes, i.e., from basaltic andesite to rhyolite. According to Klaver et al. (2016), they reflect the progressive magmatic differentiation of an Al-rich hydrous mafic melt from a lower crustal reservoir to the upper magma chamber.

Petrology and geochemistry

The petrological and geochemical diversity of the samples illustrates a complex magmatic history. Mafic enclaves with chilled margins in intermediate-to-felsic rocks is characteristic of injection of mafic magma into an evolved magma chamber (Fig. 2b–d), whereas samples with a trachytic composition (e.g., NA007-002c) form from magmatic differentiation of the mafic magma or mixing with the evolved magma. The basaltic andesite or andesite composition of the mafic enclaves indicates that their parent melt is not a direct product of mantle melting, but already has started to differentiate in a deeper magma chamber before reaching the shallower, evolved magma chamber. This is consistent with the compatible element-depleted nature of the most mafic rocks (as observed in the whole rock trace element data), likely a result of fractionate magmatic differentiation (Fig. 4). Slightly lower Ti and V relative to mid-ocean ridge basalt (MORB) may be the result of early magnetite crystallization, whereas lower Au, Co, Cu, and Ni contents likely reflect early sulfide formation. Partitioning of Ni ± Co in olivine (Spandler and O'Neill 2010) throughout wherlite formation during the early magmatic differentiation history (Klaver et al. 2016) may also account for their higher depletion in basaltic andesite in regard to other siderophile and chalcophile elements (Fig. 4). The high As, Ag, Sb, Tl, and Pb contents in the basaltic andesite relative to MORB may either be related to early differentiation, as these elements are mostly incompatible (Fig. 4), or to mantle enrichment due to supra-subduction zone contamination by slab dehydration, particularly for As, Sb, and Pb (Hattori et al. 2005; Patten et al. 2017).

Melt evolution modelling

The best fit parameters of fO_2 FMQ + 1 and 2 wt% H_2O are within the range given for other arc volcanic systems (i.e., ΔFMQ ≈ + 1 ± 1) where the mantle source is relatively more oxidized than in mid-ocean ridge setting (Bucholz and Kelemen 2019; Richards 2015). The modelled evolution of the SiO_2, TiO_2, Al_2O_3, CaO, and K_2O contents with decreasing MgO, or increasing differentiation, fit well with sample compositions (Fig. 3). The modelled FeO content is slightly higher as measured in the samples during the early differentiation stages (> 2 wt% MgO), possibly due to model limitations preventing simulation of early magnetite formation (Fig. 3). The modelled P_2O_5 content increases with progressive differentiation but decreases in the geochemical data (Fig. 3). This discrepancy is caused by apatite crystallization and fractionation that is not supported by the modelling. Apatite crystallization is contemporaneous with magnetite formation (Fig. 2e), leading to decreasing P_2O_5 contents in the melt as magnetite crystallization increases (cf. Jenner et al. 2010). The Na content in the modelled melt reproduces the sample composition during differentiation until 0.5 wt% MgO, then it decreases as albite forms. Conversely, Na contents remain constant in the samples with MgO < 0.5 wt%, indicating that plagioclase did not fractionate during late differentiation. Except for the minor limitations discussed above, the model describes reasonably well the sample geochemistry. The key pieces of information that can be drawn from the model is increased magnetite formation below 2.5 wt% MgO and water saturation at ~ 0.9 wt% MgO.

Controlling magmatic processes

Continuous magnetite crystallization or magnetite crisis?

The magnetite crisis, as defined by Jenner et al. (2010), refers to chemical changes in the melt related to sudden magnetite crystallization during melt differentiation at ~ 2.5 wt% MgO and is a critical mechanism to mobilize chalcophile elements during arc magma evolution. Formation of magnetite drives redox in the melt toward reduced conditions by incorporating two atoms of Fe^{3+} for one of Fe^{2+} in its crystal lattice. This favors sulfide saturation and chalcophile element partitioning from the silicate melt into sulfide phases (Jenner et al. 2010). Magnetite crisis is generally expressed in the melt chemistry by a sharp drop in FeO_2, TiO_2, and V/Sc. Limitations of the model preventing magnetite formation at MgO > 2.5 wt% cause modelled FeO_2 and TiO_2 contents and V/Sc values to increase during

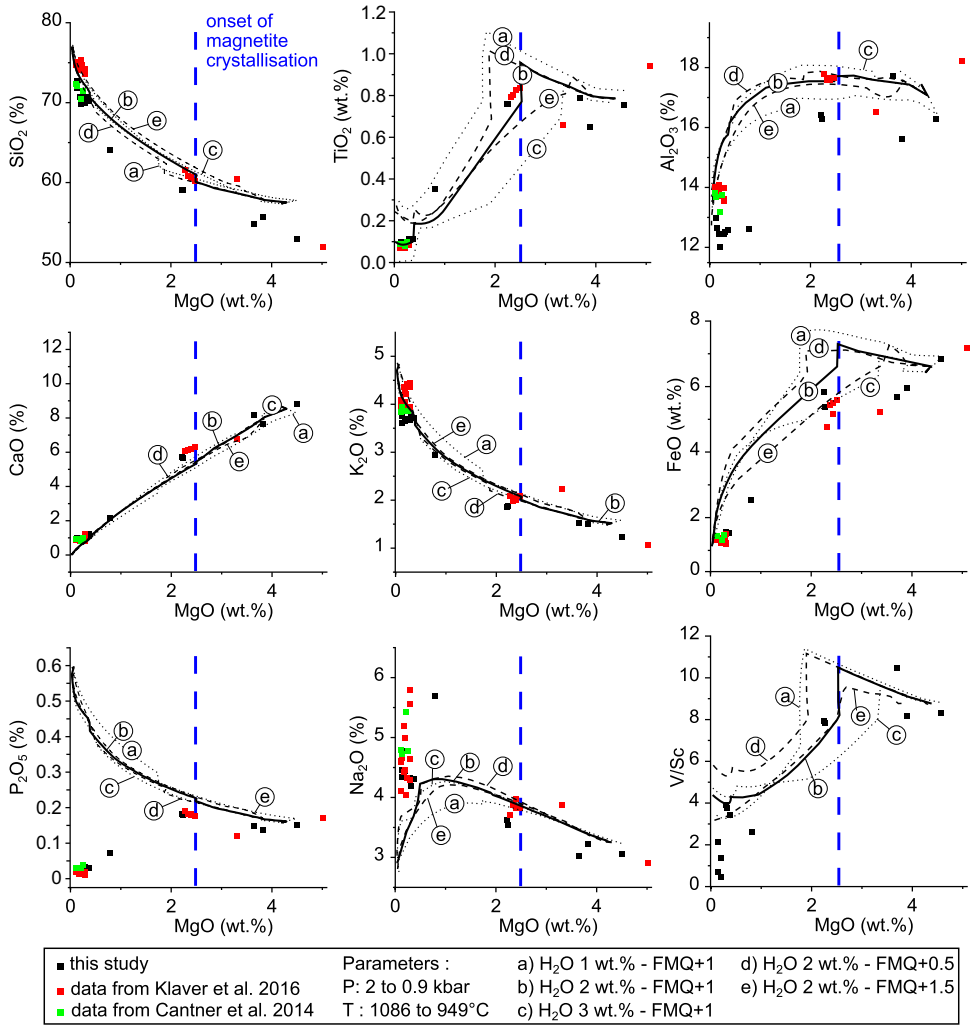

Fig. 3 Geochemical melt evolution modelled using COMAGMAT 3.75 (Ariskin and Barmina 2004) for different H_2O content and fO_2 values compared to whole rock data

magmatic differentiation (Fig. 3). Whole rock data, however, display continuously decreasing FeO_2 and TiO_2 contents and V/Sc values with magmatic differentiation until 2.5 wt% MgO, indicating early igneous magnetite formation, in accordance with petrographic observation (Figs. 2e, 3, and 5a). Below 2.5 wt% MgO, FeO_2 and TiO_2 contents decrease strongly, reflecting increased magnetite formation, as supported by modelling (Fig. 3). In addition, a drop in the V/Sc value is a good proxy for magnetite formation because V is more compatible in magnetite than Sc (Dare et al. 2014; Jenner et al. 2010). Early magnetite will have a higher V/Sc value than magnetite forming at a later stage of magmatic differentiation. Decreasing V/Sc values in igneous magnetite supports magnetite fractionation upon magmatic differentiation and suggests that magnetite reflects the composition of the melt in which it crystallizes (Fig. 5b). For magnetite hosted in rhyolite, a few grains have higher V/Sc values indicating that these are exogenous and formed from a more mafic melt (Fig. 5b). In summary, it seems that Kolumbo's magma undergoes continuous magnetite crystallization from the early stages of its differentiation history, with the rate increasing notably below 2.5 wt% MgO.

Sulfide saturation

Sulfur concentration at sulfide saturation (SCSS) during magmatic differentiation is modelled using the method developed by Smythe et al. (2017) with a melt composition calculated by COMAGMAT 3.75. In comparison to SCSS values modelled for MORB (cf. Jugo 2009; SCSS = 2000 $\mu g \cdot g^{-1}$ S), the SCSS in Kolumbo's most primitive melts is relatively low (~ 300 $\mu g \cdot g^{-1}$ S) and indicates that the melt is sulfide-saturated during the entire differentiation process (Fig. 5c). The presence of sulfides in all samples supports sulfur saturation throughout the differentiation process and their habit (i.e., droplets and blebs) indicates crystallization from a

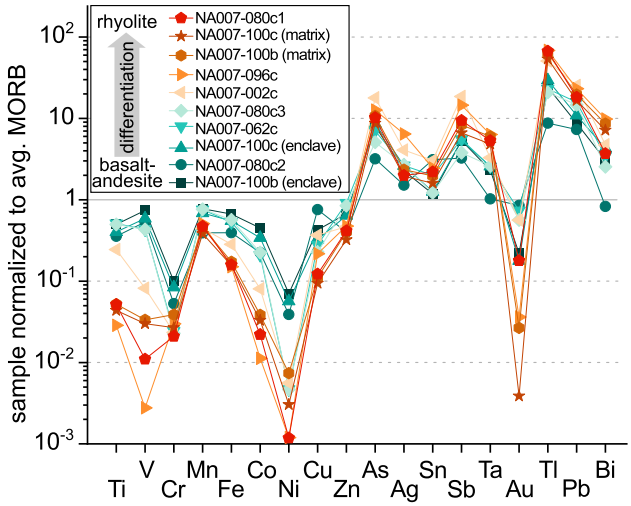

Fig. 4 Whole rock trace element data normalized to average mid-oceanic ridge basalt, based on Arevalo and McDonough (2010)

sulfide liquid (Fig. 2e–k) (Patten et al. 2013). Samples with compositions between 2.0 and 4.0 wt% MgO have S values below the SCSS (Fig. 5c) despite the presence of sulfide droplets in the matrix and inclusions in phenocrysts (Fig. 2e, i, k). This apparent low S content is likely the result of S loss by degassing upon eruption, while outlying high S values (i.e., > 500 $\mu g \cdot g^{-1}$) in felsic samples are explained by seawater/rock interaction upon eruption (Brandl et al. 2022). The mechanisms triggering early sulfide saturation are unclear but may be related to magnetite or amphibole crystallization (Georgatou et al. 2022; Jenner et al. 2010). Similarly, amphibole replacing clinopyroxene modifies the redox state of the melt and may trigger sulfide saturation as the primitive basaltic melt evolves toward an andesite composition in the lower crustal reservoir (Georgatou et al. 2021, 2022). This process is however not clearly identified in Kolumbo.

Degassing

Understanding the degassing processes at Kolumbo is critical for understanding metal transfer in the magmatic-hydrothermal system given that degassing volatiles can carry and transport ligands and metals (Hedenquist and Lowenstern 1994). However, the initial volatile content of the samples may be altered by eruption degassing and interaction with seawater (Fig. 5c). Thus, the best proxy to assess degassing is to use water saturation indicated by the modelling of the melt evolution (i.e., 0.9 wt% MgO). However, initial volatile content in the model (2 wt% H_2O) is lower than the average loss on ignition measured (3.2 wt%) in the most mafic samples (Table 1). This is likely caused by seawater/rock interaction after eruption increasing the volatile content in the samples in regard to their pre-eruption values (Coogan and Gillis 2018; Haraguchi et al. 2014). Loss on ignition values for rhyolite yield a post-water saturation volatile content of 2.8 wt% in lava, which is nicely reproduced by the model but increasing up to 7.1 wt% in pumices. However, as pumice forms during the eruption as a mixture of degassing volatiles and magma, it may not be representative of the initial volatile content. Degassing of magmatic volatile species is controlled by the confining pressure, temperature, oxidation state, and volatile content in the magma. Usually, magmatic volatiles are released in the following order: $CO_2 < SO_2$-$H_2S < H_2O$ (and halogens), according to their solubility in the melt (Mavrogenes and O'Neill 1999; Rouwet et al. 2019). As CO_2 is saturated early in magmatic arc systems, it starts to separate from the silicate melt in the lower crust (Lowenstern 2001). In the case of Kolumbo, CO_2 effervescence likely occurs in the lower crust where differentiation from basalt to basaltic andesite occurs. Our model predicts water saturation at 0.9 wt% MgO (i.e., during trachyte formation) in the upper magma chamber (between 7 and 2 km depth). This indicates that SO_2 degassing could have taken place during magma ascend, or in the upper magma chamber. However, early sulfide saturation might have prevented SO_2 degassing by sequestrating S in a solid or liquid sulfide phase. As the magma degasses, volatile bubbles can nucleate on sulfide phases, leading to the formation of sulfide-volatile compounds (Barnes et al. 2019; Mungall et al. 2015).

Metal flux during melt evolution

Pre-water saturation magmatic differentiation

Whole rock data indicate that before water saturation is reached during magmatic differentiation, V, Ni, Co, Cu, Ti, Au, and Zn are progressively depleted, whereas Sn, Ag, As, Sb, Pb, and Tl are enriched (Fig. 6a–f; Table 2). Depletion in V, Ni, Co, and to some extent Fe and Ti is related to magnetite crystallization and settling (c.f. Dare et al. 2014). Despite early sulfide saturation, there is no notable chalcophile element depletion in the magma before rhyolite formation and water saturation, implying more complex processes during the magmatic evolution than simple sulfide phase formation and settling (Fig. 6a–d, Table 2).

Insight from magnetite before water saturation

Magnetite in Kolumbo's volcanic rocks is of magmatic origin and almost exclusively primary (Fig. 5a, b). Thus, magnetite trace element compositions reflect the metal content in the melt, whereas the whole rock composition is considered representative of the magma (i.e., melt plus mineral phases) composition. The contrasting metal content between magnetite and its host rock provides first-order insights into metal mobilizing processes during magmatic

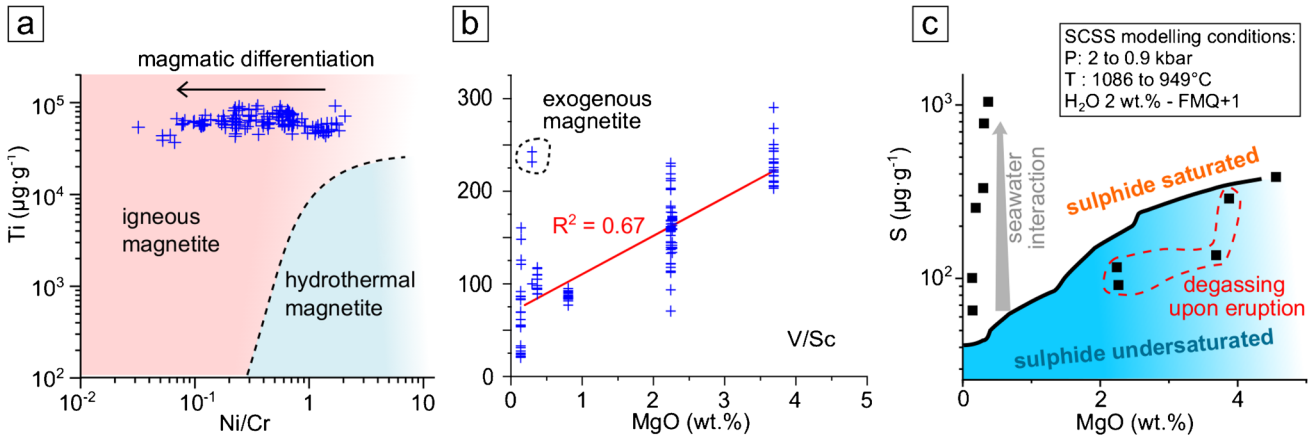

Fig. 5 **a** Classification into magmatic and hydrothermal magnetite based on Dare et al. (2014); **b** V/Sc in magnetite compared to the MgO content of the whole rock. **c** Modelling of the sulfur concentration at sulfide saturation (SCSS) versus MgO content in the melt during magmatic differentiation compared to S content versus MgO content of the whole rock (after Smythe et al. 2017, using modelled melt composition)

differentiation (Table 4). From basaltic andesite through trachyte differentiation stages, the Cu content in the magma shows a slightly decreasing trend but remains almost constant (avg. 28 $\mu g \cdot g^{-1}$) while it decreases from an average of 141 to 10 $\mu g \cdot g^{-1}$ in the corresponding magnetite (Fig. 6a). While Cu remains in the magma, its availability in the melt for magnetite decreases during magmatic differentiation. This indicates that the majority of Cu is sequestered in mineral phases, likely sulfide phases that predominantly stay in the magma. Nickel and Co show a different behavior. Nickel is depleted simultaneously in magnetite and in the magma during magmatic differentiation (Fig. 6e). This indicates that, unlike any sulfide phases, magnetite fractionates from the magma after crystallizing (Fig. 7a stage 1). Cobalt is less compatible than Ni in magnetite and is consequently slightly less depleted in the magma as magnetite fractionates (Fig. 6f) (Dare et al. 2014).

Metal budget at sulfide saturation

At the Kolumbo volcano, the melt is sulfide-saturated at least from the basaltic andesite differentiation stage on, as observed petrographically and supported by the modelling (Figs. 2e–k and 5c). A consistent drop in the Cu/Ag value during differentiation indicates monosulfide solid solution (MSS) formation from a sulfide liquid or precipitation of Cu-rich sulfide (Figs. 2e–k and 8) (Du and Audétat 2020; Jenner et al. 2010, 2015). Despite early sulfide saturation, chalcophile elements in the whole rocks are not significantly depleted during magmatic differentiation and are even enriched for Ag, As, Au, Bi, Cu, Hg, Pb, Sb, Sn, and Tl prior to water saturation, indicating that most sulfides phases do not settle and remain in suspension in the magma during differentiation (Figs. 6a–d and 7a stage 1; Table 2). This is likely linked to the increasing melt viscosity as it differentiates and limited size of the sulfide phases (i.e., < 10 µm for disseminated sulfides; Fig. 2k) which both drastically reduce the settling velocity (< 1 cm.year^{-1} for micrometer-scale sulfides; see Holzheid 2010). Settling of sulfides phases can also be prevented by the formation of sulfide-volatile compounds as the magma degasses (Mungall et al. 2015; Yao and Mungall 2020). That is, as a volatile bubble grows on a sulfide liquid droplet, the average buoyancy of the compound can eventually lead it to "float" in the melt or to rise upward (Yao and Mungall 2020).

Metal mobility upon degassing

Magmatic degassing is an efficient process to mobilize metals from a magmatic melt and transport them as sulfide or chloride complexes (Gammons and Williams-Jones 1997; Nadeau et al. 2021). At Kolumbo, according to modelling, water saturation is reached at 0.9 wt% MgO during the trachyte differentiation stage. Previous degassing that could have occurred during magmatic differentiation (i.e., of CO_2, SO_2, H_2S) did not significantly deplete chalcophile elements in the magma prior to water saturation (Fig. 6a–d; Table 2).

A first-order insight of metal mobility upon volatile degassing is given by comparing the metal content in the "degassed" samples (i.e., after water saturation) with "undegassed magma." The evolution of metal content in "undegassed magma" is extrapolated for compositions < 0.9 wt% MgO using a curve fitting pre-water saturation data (i.e., > 0.9 wt% MgO). It appears that the most chalcophile

elements such as Ag, Au, Cu, and Hg (with the notable exception of Bi and Tl), as well as less chalcophile elements like As, Pb, Sb, Sn, and Zn, are depleted in the samples after water saturation in comparison to the "un-degassed magma" (Figs. 6a–d and 7a stage 2, b). Chalcophile elements are mostly enriched in sulfide phases prior to water saturation, and therefore, their depletion in the "degassed" samples implies metal transfer between the sulfide phases and the volatiles. Although Ni and Co are not depleted in comparison to "un-degassed magma," their content in the magma continues to decrease after water saturation (Fig. 6e, f). The progressive loss of Ni and Co is probably controlled by continuous magnetite crystallization and fractionation (Fig. 7a stage 2, b). Formation of sulfide-volatile compounds may lead to the oxidation and resorption of the sulfide phase, transferring the metals to the volatiles and contributing to the formation of a metal-rich fluid (Edmonds and Mather 2017; Mungall et al. 2015).

Magnetite as metal flux tracer

The different compatibility of chalcophile elements in sulfides, volatile phases, and magnetite allows tracking metal mobilization during magmatic differentiation. Given that igneous magnetite at Kolumbo is primary, the V/Sc value of the magnetite allows tracking of the degree of magmatic differentiation and can be calibrated with the whole rock compositions of the host rock (Fig. 9). Decreasing Cu contents in magnetite during magmatic differentiation and before water saturation reflects sulfide saturation (Fig. 9). High Cu contents but low V/Sc values are characteristic of post-degassing magnetite that formed after water saturation (Fig. 9). Following degassing, chalcophile elements are locally enriched within magnetite (Figs. 2g and 6a, b). This behavior is the result of the competing partitioning of chalcophile elements between sulfides and magnetite. With S absent from the melt after degassing, remaining chalcophile elements that did not partition into volatiles are then incorporated into the magnetite (Fig. 7a stage 3, b).

Comparison with other arc volcanoes

Sulfide saturation, formation, and fractionation of sulfide phases and volatile degassing are among the main processes controlling chalcophile element contents in the melt during magmatic differentiation (Edmonds and Mather 2017; Jenner et al. 2010, 2015; Patten et al. 2013). The

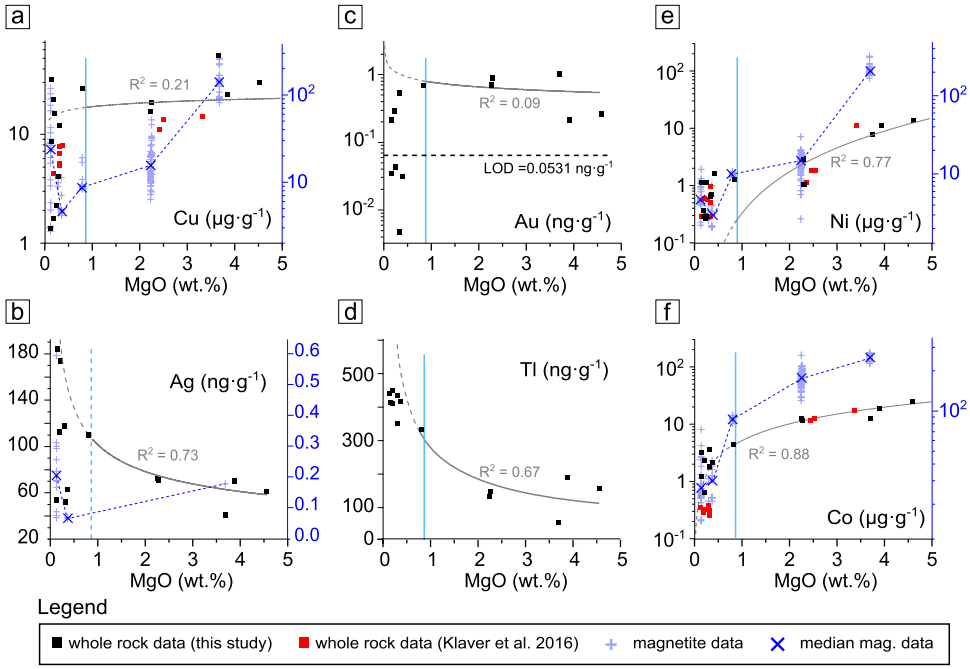

Fig. 6 Chalcophile and siderophile element contents of whole rocks and magnetite during differentiation as shown by whole rock MgO data. The left and right axes are for the whole rock and magnetite data, respectively. Note: scale of whole rock and magnetite data are different. The blue dotted lines connect the medians of the magnetite data. The vertical blue lines represent water saturation at 0.9 wt% MgO according to modelling. Fitting curves (in gray) are calculated based on data > 0.9 wt% MgO (i.e., before water saturation) and indicate the evolution of metal content in the whole rock during magmatic differentiation. The dotted segments of the curves are extrapolated toward MgO = 0 wt% to simulate the evolution of metal content in the whole rock during magmatic differentiation, in the absence of water saturation, degassing, and associated metal removals

whole rock Cu/Ag value compared to the MgO content illustrates how chalcophile elements are mobilized, highlighting whether or not a sulfide liquid or crystalline sulfide phase forms at sulfide saturation (Du and Audétat 2020; Jenner et al. 2010; Li and Audétat 2012; Patten et al. 2013). Formation of a sulfide liquid does not change the Cu/Ag value, as both elements have similar partition coefficient in sulfide liquid (Li and Audétat 2012; Patten et al. 2013). Conversely, crystallization of sulfides (i.e., MSS or Cu-rich sulfides) leads to a decrease of the Cu/Ag value because Cu is more compatible than Ag in these phases (Du and Audétat 2020; Jenner et al. 2015; Li and Audétat 2012). In a basalt, for example, the Cu/Ag value is usually close to the mantle value of ~ 3000 ± 500 and remains unchanged during magmatic differentiation, provided only sulfide liquid forms (e.g., at Niuatahi volcano; Fig. 8) (Brandl et al. 2022; Park et al. 2015; Wang et al. 2019). Crystallization and fractionation of sulfides lead to a progressively decreasing Cu/Ag value from the mantle value in the whole rock during magmatic differentiation, as observed in samples from the Manus and Lau basin of the Valu Fa Ridge (Tonga), Brothers volcano, and adjacent ridges of the Kermadec arc (Fig. 8) (Brandl et al. 2022; Jenner et al. 2010, 2012, 2015).

The Cu/Ag values of Kolumbo samples reflects a differentiation process similar to the early differentiation stages of the Nisyros volcano (Georgatou et al. 2022). The Cu/Ag values at Kolumbo are interpreted to yield mantle-like ratio at basaltic composition and decrease continuously until ~ 0.9 wt% MgO, indicating uninterrupted formation of magmatic sulfides since early differentiation in the lower crust until the trachyte/rhyolite stage in the upper magma chamber (Fig. 8). Degassing at ~ 0.9 wt% MgO leads to a sharper drop of the Cu/Ag value,

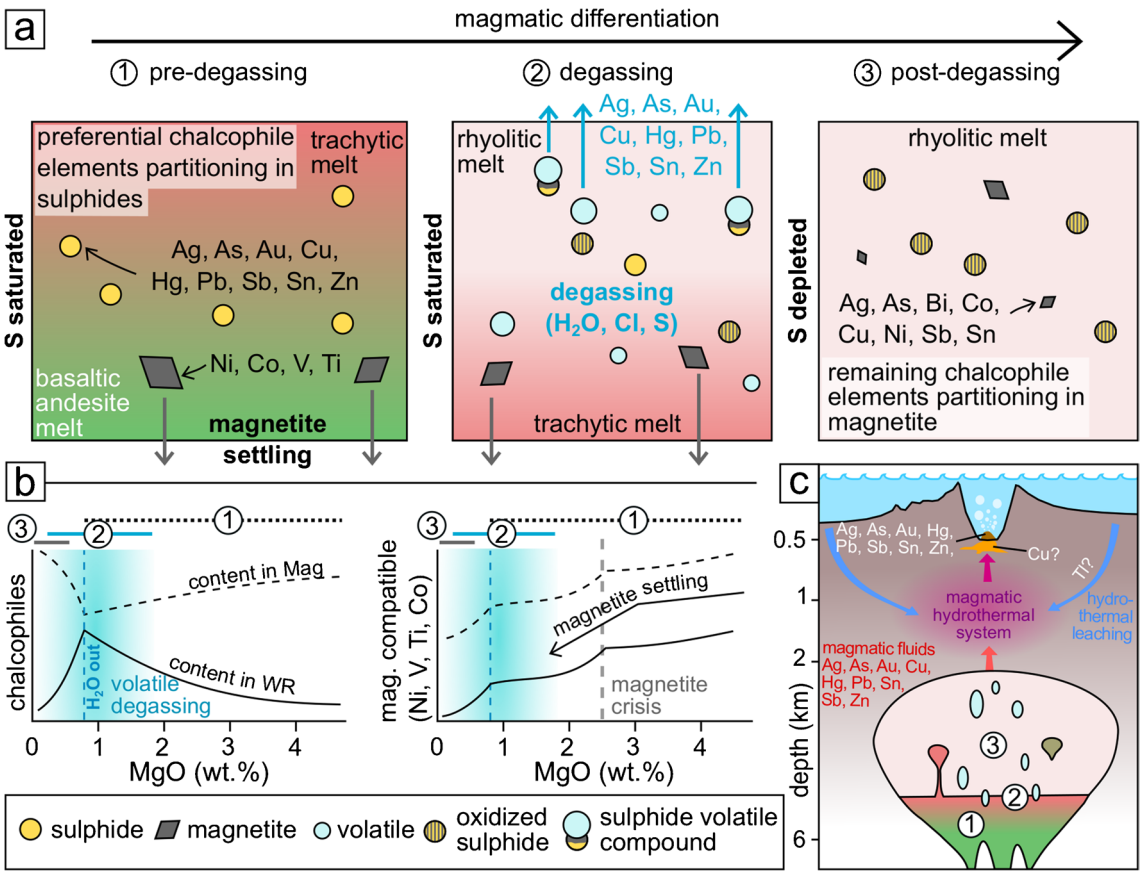

Fig. 7 Conceptual model of metal mobility during magmatic differentiation and related hydrothermal processes. **a** 1. Before degassing, the melt is S-saturated, chalcophile elements (i.e., Ag, As, Au, Cu, Hg, Sn, Sb, Pb, and Zn) fractionate preferably into sulfide phases while Ni, Co, V, and Ti are partitioned preferably into magnetite. The sulfide phases are "floating" in the magma while magnetite settles. 2. Upon degassing, the sulfide phases are oxidized by the formation of sulfide-volatile compounds or interaction with volatiles. Chalcophile elements are removed from the sulfides and likely transported as S- or Cl-complexes. 3. After degassing, the system is S-depleted and the remaining chalcophile elements in the melt partition into magnetite, locally forming chalcophile-element-rich magnetite. **b** Chalcophile and magnetite-compatible elements in whole rock and magnetite during differentiation. **c** Model of metal transfer within Kolumbo's magmatic-hydrothermal system

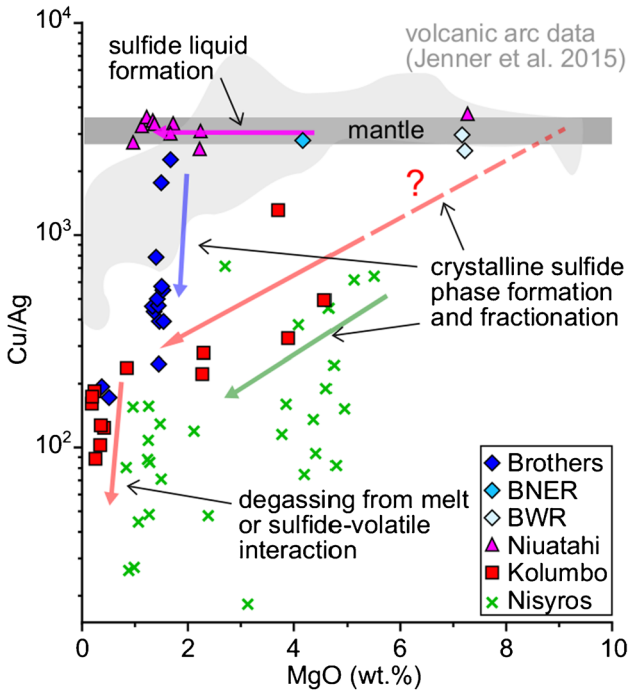

Fig. 8 Evolution of Cu/Ag compared to MgO content in volcanic rock samples of different arc volcanoes. Niuatahi data are from Park et al. (2015) and Wang et al. (2019), Brothers volcano, Brothers northeast ridge (BNER), and Brothers west ridge (BWR) data are from Brandl et al. (2022), and Nisyros data are from Georgatou et al. (2022). According to Brandl et al. (2022), basalt from the BWR and basaltic andesite from BNER are considered as parental melt analogues for the Bothers dacite

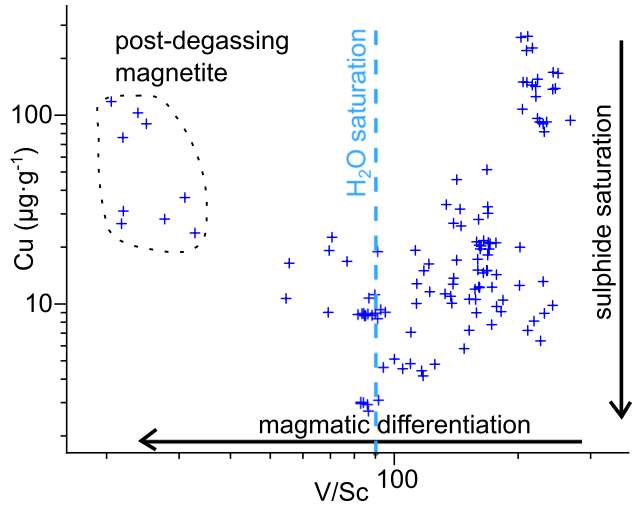

Fig. 9 Cu content in igneous magnetite compared to its V/Sc value. Water saturation is given by COMAGMAT 3.75 modelling and placed on the V/Sc axis after calibration with the composition of magnetite's host-rock

indicating mobilization of Cu by magmatic fluids as Cu is more compatible than Ag in a volatile phase exsolving from the melt (Fig. 8) (Audétat and Edmonds 2020).

Mineralizing magmatic-hydrothermal system at Kolumbo

Metal sources

Deep hydrothermal fluid circulation in the oceanic crust is an efficient process for mobilizing metals from the country rocks and partially controls the metal endowment in SMS/VMS deposits (Hannington et al. 2005). In mid-oceanic ridge settings, the oceanic crust is thought to represent the source of metals (i.e., As, Au, Cu, Pb, Se, Sb, and Zn) that are mobilized by hydrothermal leaching (Brauhart et al. 2001; Patten et al. 2016; Skirrow and Franklin 1994). Similarly, in volcanic arc environments, especially in continental crust, felsic country rocks are enriched in Ag, As, Pb, Sb, Sn, and Tl compared to MORB (Fig. 4), and may be a source for these elements that are commonly enriched in related SMS/VMS deposits (Hannington et al. 2005; Shikazono 2003; Shu et al. 2022; Stanton 1994). At Kolumbo, the sulfide-sulfates chimneys are Zn-Pb-rich with relatively high As, Ag, Au, Hg, Sb, and Tl contents, but are relatively Cu poor (Kilias et al. 2013). Recent study of δ^{65}Cu in sulfide minerals of the chimneys supports significant magmatic contributions (i.e., δ^{65}Cu range of ~ 0‰) and strongly suggests that direct magmatic degassing supplies volatiles and Cu to the hydrothermal system at Kolumbo (Zegkinoglou et al. 2023). These findings are concordant with Cu depletion during magmatic differentiation, interpreted as loss during volatile degassing and suggest that As, Ag, Au, Hg, Pb, Sb, Sn, and Zn are mobilized in the same way (Fig. 10). Conversely, Tl is enriched in Kolumbo's chimneys but does not seem to be mobilized during degassing, which suggests that metal sources other than the magma are involved in the magmatic-hydrothermal system (Figs. 6d and 10). Similar metal enrichment has been linked to magmatic contribution to hydrothermal systems in other volcanic arc SMS, especially at the extensively studied Brothers volcano (Berkenbosch et al. 2015, 2019; de Ronde et al. 2011, 2019). In Brothers chimneys, high enrichment factors of Ag, Au, and Cu with regard to the host rock indicate a magmatic source, whereas those of As, Pb, Sb, Sn, Tl, and Zn are closer to host rock values, pointing toward a mixed magmatic and host rock source (Berkenbosch et al. 2019). Thus, the metal association at Kolumbo likely results from a combination of hydrothermal wall rock leaching and magmatic input—i.e., magmatic volatiles and/or hypersaline brines (see de Ronde et al. 2019; Diehl et al. 2020)—(Fig. 7c, 10). Constraining metal sources is fundamental to understand the formation of SMS, but it is crucial to also consider the magmatic-hydrothermal processes that may affect the metal content in the mineralizing fluid and ultimately the metal association in the chimneys.

Magmatic-hydrothermal control on metal association

Submarine arc volcanoes host complex and dynamic magmatic-hydrothermal systems with constantly evolving fluid chemistry through space and time (Diehl et al. 2020; Lee et al. 2023; Lilley et al. 2003). Magmatic-hydrothermal processes occurring on and below the seafloor (e.g., phase separation, transient magmatic input, and mixing with brines) may drastically affect the metal content of the fluids (Diehl et al. 2020; Hannington 2014). Despite Cu being mobilized during degassing, it is not strongly enriched in the hydrothermal chimneys at Kolumbo, suggesting that Cu may be trapped in the deeper/hotter parts of the hydrothermal system (Fig. 10). We identify four mechanisms that may impact the metal content in the mineralizing fluid: cooling, boiling, phase separation, and fluid mixing.

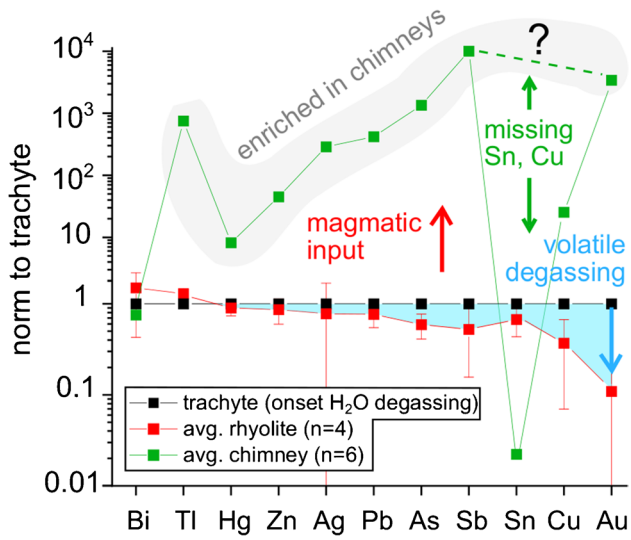

Fig. 10 Average metal content in Kolumbo's sulfide-sulfate chimneys and volcanic samples, normalized to trachyte. The trachyte composition corresponds to the onset of water saturation and degassing. Please note that the vertical scale is increased below 1. Nickel and Co are not shown here because of their siderophile nature and strong partitioning in magnetite, causing depletion between trachyte and rhyolite that is not related to degassing

1) Metal zoning is common in VMS deposits and is controlled by temperature-dependent sulfide solubility. Copper requires temperatures above 300 °C for significant transport in typical VMS hydrothermal fluid, whereas Pb and Zn remain soluble at lower temperatures of ~ 180 °C (e.g., Hellyer, Rosebery, Mount Chalmer, and Scuddles VMS deposits, Australia; Large 1992). The venting hydrothermal fluids at Kolumbo are as high as 265 °C (Nomikou et al. 2022). Thus, the Zn-Pb(-Au) sulfide-sulfate chimneys represent the cooler part of the system, and Cu is likely trapped at depth as the temperature drops below 300 °C.
2) Boiling drastically modifies the chemistry of a hydrothermal solution (e.g., pH increase, changes in fO_2, fS_2), triggering oxide, native metals, sulfide, carbonate, and sulfate precipitation (Drummond and Ohmoto 1985; Heinrich 2007). Scales forming in boiling geothermal systems have trace element enrichments consistent with hydrothermal chimneys and reveal that Co, Cu, and Sn are deposited in the highest-temperature scales (290–345 °C), As and Ni in high- to intermediate-temperature scales, and Ag, Pb, Sb, and Zn in lower-temperature scales (220–260 °C) (Grant et al. 2020). Upon boiling, Au precipitates efficiently but is still enriched in high- to low-temperature scales as it is easily remobilized by hydrothermal fluids over a wide range of temperatures (Grant et al. 2020; Williams-Jones et al. 2009). Similarly, volatile elements (e.g., As, Sb, Se, and Te) are easily remobilized, concentrated during boiling-induced element fractionation and eventually enriched in SMS (e.g., Niua South, Tonga; Falkenberg et al. 2021). At Kolumbo, magmatic fluid mixes with seawater-derived hydrothermal fluids at a depth of 1160 mbsl (i.e., 650 m below the seafloor) and a temperature of 270 °C (Rizzo et al. 2019). Under these conditions, the magmatic-hydrothermal fluid is very close to boiling (Bischoff and Rosenbauer 1984) and eventually does as it ascends toward the seafloor. This is supported by the extreme Cu isotope fractionation in the minerals of the chimneys (Zegkinoglou et al. 2023). Boiling-induced precipitation of chalcopyrite and other sulfides at depth may explain the lack of Cu and Sn observed in the chimneys, despite mobilization during magmatic degassing (Figs. 6a and 10; Table 2).
3) Magmatic degassing generates a single-phase liquid of relatively low salinity (2–10 wt% NaCl eq.), which tends to separate into a hypersaline brine (40 to > 60 wt% NaCl eq.) and a vapor phase as it decompresses (< 4 km depth) and cools (Sillitoe 2010 and references therein). Phase separation causes metal fractionation with Zn, Ag, Sn, Pb, and Tl partitioning into the brine and As, Au, and Cu into the vapor (Heinrich et al. 1999). In porphyry Cu systems, Cu sulfides precipitate upon fluid cooling over the 425 to 350 °C range, assisted by fluid-rock interaction (Sillitoe 2010 and references therein). Similar processes at Kolumbo may lead to formation of Cu porphyry-style mineralization at depth, which later remobilization by magmatic-hydrothermal fluids could provide metals to the chimneys (Martin et al. 2023).
4) Submarine magmatic-hydrothermal systems are complex systems hosting various fluids of diverse origins: i.e., seawater—eventually modified by fluid-rock interaction—connate brines, magmatic-derived vapor, and brines (Diehl et al. 2020; Hannington et al. 2005). Magmatic brines can form lenses and be stored in the permeable sub-surface for hundreds of thousands of years

(Afanasyev et al. 2018). Changes in the hydrothermal fluid regime may lead to interaction of seawater with these metal-rich fluids, providing metals for the formation of chimneys on the seafloor (de Ronde et al. 2019). Lenses of fluids trapped in the volcaniclastic sequence at Kolumbo have been identified (Hübscher et al. 2015) and may represent magmatic brines. Mixing of such fluids with hydrothermal fluids could contribute to the Ag, Pb, and Zn enrichments observed in the chimneys, as these metals preferentially partition into brine during magmatic fluid phase separation (Heinrich et al. 1999).

The metal association observed in chimneys at Kolumbo corresponds to low-temperature VMS deposits (< 300 °C), which usually show enrichment in Zn, Pb, Ag, Au, Cd, Sn, Sb, As, Hg, ± Tl, and ± W (Hannington 2014). The high contents of As, Sb, Hg, and Tl in the chimneys support boiling and zone refining processes, as these elements are easily mobilized in the vapor phase (Hannington 2014). However, the metal content of the chimneys likely does not reflect a straight forward process as the evolving dynamic nature of submarine magmatic-hydrothermal systems could include periods of magmatic quiescence that results in a seawater-dominated hydrothermal fluid, whereas periods of intense magmatic activity would increase the proportion of magmatic fluids (Diehl et al. 2020). Tectonic or magmatic events, changes in permeability may affect the dynamics of the hydrothermal fluid regime, leading to mobilization of different fluids and ultimately impacting the metal budget (de Ronde et al. 2019). Finally, eventual mineralization caused by the different processes discussed above may be overprinted by later hydrothermal fluid circulation, eventually remobilizing the metals toward the seafloor (Martin et al. 2023).

Conclusions

The Kolumbo submarine arc volcano and its SMS are an ideal setting to investigate magmatic processes and metal transfer mechanisms in a mineralizing magmatic-hydrothermal system. Combining in situ magnetite trace element contents with whole rock data and modelling provides information on metal behavior in the magma during differentiation. Our data indicate that early and long-lasting sulfide saturation in the magma at Kolumbo leads to the partitioning of chalcophile elements into sulfide phases with limited settling. We suggest that most of the sulfides remain in the magma, either because of their small size (< 10 µm) and high viscosity of the magma, or because of sulfide-volatile compounds formation. Upon degassing, As, Ag, Au, Cu, Hg, Sb, Sn, Pb, and Zn are depleted in the magma, likely partitioning into the volatile phase, either from the melt or during sulfide oxidation by volatiles. After degassing, the remaining chalcophile elements in the melt are incorporated into magnetite as the melt becomes sulfur undersaturated. The metals lost during magmatic degassing are enriched in the mineralization, suggesting a magmatic origin. Chimneys at Kolumbo are also enriched in Tl, which is not depleted in the magma during degassing, and reflect that other metal sources and processes, such as leaching of country rocks, may contribute to the metal budget. Our study shows that trace element contents in igneous magnetite are a powerful tool in tracking metal behavior during magmatic differentiation, identifying sulfide saturation in the melt, and discriminating between pre- and post-degassing magnetite.

Supplementary information.

Supplementary Information The online version contains supplementary material available at https://doi.org/10.1007/s00126-024-01262-7.

Acknowledgements K.L.C. Bell and S. Carey are greatly acknowledged for operational support and their participation in data collection. The officers and the crew of the E/V *Nautilus* are gratefully acknowledged for their important and effective contribution to the field work and sampling.

Funding Open Access funding enabled and organized by Projekt DEAL. This work is funded by the German Research Foundation (DFG-SPP Program DOME grant PA 3523/2–1 and INST 121384/213–1 FUGG). This work was supported by the Institute for Exploration (IFE-USA) and the collaborative project "New Frontiers in the Ocean Exploration 2010" between the Graduate School of Oceanography at the University of Rhode Island (URI-USA) and the Faculty of Geology & Geoenvironment, (NKUA). PN acknowledges support by the SANTORY program which is funded by the Hellenic Foundation for Research and Innovation (HFRI) (Grant Number 1850).

Declarations

Competing interests The authors declare no competing interests.

Open Access This article is licensed under a Creative Commons Attribution 4.0 International License, which permits use, sharing, adaptation, distribution and reproduction in any medium or format, as long as you give appropriate credit to the original author(s) and the source, provide a link to the Creative Commons licence, and indicate if changes were made. The images or other third party material in this article are included in the article's Creative Commons licence, unless indicated otherwise in a credit line to the material. If material is not included in the article's Creative Commons licence and your intended use is not permitted by statutory regulation or exceeds the permitted use, you will need to obtain permission directly from the copyright holder. To view a copy of this licence, visit http://creativecommons.org/licenses/by/4.0/.

References

Afanasyev A, Blundy J, Melnik O, Sparks S (2018) Formation of magmatic brine lenses via focussed fluid-flow beneath volcanoes. Earth Planet Sci Lett 486:119–128

Agostini S, Doglioni C, Innocenti F, Manetti P, Tonarini S (2010) On the geodynamics of the Aegean rift. Tectonophysics 488:7–21

Arevalo R, McDonough WF (2010) Chemical variations and regional diversity observed in MORB. Chem Geol 271:70–85

Ariskin AA, Barmina GS (2004) COMAGMAT: development of a magma crystallization model and its petrological applications. Geochem Int 42:1–157

Audétat A (2019) The metal content of magmatic-hydrothermal fluids and its relationship to mineralization potential. Econ Geol 114:1033–1056

Audétat A, Edmonds M (2020) Magmatic-Hydrothermal Fluids. Elements 16:401–406

Barnes SJ, Le Vaillant M, Godel B, Lesher CM (2019) Droplets and bubbles: solidification of sulphide-rich vapour-saturated orthocumulates in the Norilsk-Talnakh Ni–Cu–PGE ore-bearing intrusions. J Petrol 60:269–300

Berkenbosch HA, de Ronde CEJ, Gemmell JB, McNeill AW, Goemann K (2012) Mineralogy and formation of black smoker chimneys from Brothers submarine volcano, Kermadec arc. Econ Geol 107:1613–1633

Berkenbosch HA, de Ronde CEJ, Paul BT, Gemmell JB (2015) Characteristics of Cu isotopes from chalcopyrite-rich black smoker chimneys at Brothers volcano, Kermadec arc, and Niuatahi volcano, Lau basin. Miner Deposita 50:811–824

Berkenbosch HA, de Ronde C, Ryan CG, McNeill AW, Howard DL, Gemmell JB, Danyushevsky LV (2019) Trace element mapping of copper- and zinc-rich black smoker chimneys from Brothers volcano, Kermadec arc, using synchrotron radiation XFM and LA-ICP-MS. Econ Geol 114:67–92

Bischoff JL, Rosenbauer RJ (1984) The critical point and two-phase boundary of seawater, 200–500°C. Earth Planet Sci Lett 68:172–180

Blanks DE, Holwell DA, Fiorentini ML, Moroni M, Giuliani A, Tassara S, González-Jiménez JM, Boyce AJ, Ferrari E (2020) Fluxing of mantle carbon as a physical agent for metallogenic fertilization of the crust. Nat Commun 11:4342

Brandl PA, Portnyagin M, Zeppenfeld H, Tepley FJ, de Ronde CE, Timm C, Hauff F, Garbe-Schönberg D, Bousquet R (2022) The origin of magmas and metals at the submarine Brothers volcano, Kermadec arc New Zealand. Econ Geol 118(7):1577–604

Brauhart CW, Huston DL, Groves DI, Mikucki EJ, Gardoll SJ (2001) Geochemical mass-transfer patterns as indicators of the architecture of a complete volcanic-hosted massive sulfide hydrothermal alteration system, Panorama district, Pilbara, Western Australia. Econ Geol 96:1263–1278

Bucholz CE, Kelemen PB (2019) Oxygen fugacity at the base of the Talkeetna arc, Alaska. Contrib Mineral Petrol 174:1–27

Cantner K, Carey S, Nomikou P (2014) Integrated volcanologic and petrologic analysis of the 1650AD eruption of Kolumbo submarine volcano, Greece. J Volcanol Geoth Res 269:28–43

Carey S, Nomikou P, Bell KC, Lilley M, Lupton JE, Roman C, Stathopoulou E, Bejelou K, Ballard R (2013) CO2 degassing from hydrothermal vents at Kolumbo submarine volcano, Greece, and the accumulation of acidic crater water. Geology 41:1035–1038

Chrapkiewicz K, Paulatto M, Heath BA, Hooft EEE, Nomikou P, Papazachos CB, Schmid F, Toomey DR, Warner MR, Morgan JV (2022) Magma chamber detected beneath an arc volcano with full-waveform inversion of active-source seismic data. Geochem Geophys Geosyst 23:e2022GC010475

Coogan LA, Gillis KM (2018) Low-temperature alteration of the seafloor: impacts on ocean chemistry. Annu Rev Earth Planet Sci 46:21–45

Craddock PR, Bach W, Seewald JS, Rouxel OJ, Reeves E, Tivey MK (2010) Rare earth element abundances in hydrothermal fluids from the Manus Basin, Papua New Guinea: indicators of sub-seafloor hydrothermal processes in back-arc basins. Geochim Cosmochim Acta 74:5494–5513

Dare SA, Barnes S-J, Beaudoin G (2012) Variation in trace element content of magnetite crystallized from a fractionating sulfide liquid, Sudbury, Canada: implications for provenance discrimination. Geochim Cosmochim Acta 88:27–50

Dare SAS, Barnes S-J, Beaudoin G, Méric J, Boutroy E, Potvin-Doucet C (2014) Trace elements in magnetite as petrogenetic indicators. Miner Deposita 49:785–796

de Ronde CEJ, Baker ET, Massoth GJ, Lupton JE, Wright IC, Feely RA, Greene RR (2001) Intra-oceanic subduction-related hydrothermal venting, Kermadec volcanic arc, New Zealand. Earth Planet Sci Lett 193:359–369

de Ronde CEJ, Faure K, Bray CJ, Chappell DA, Wright IC (2003) Hydrothermal fluids associated with seafloor mineralization at two southern Kermadec arc volcanoes, offshore New Zealand. Miner Deposita 38:217–233

de Ronde CEJ, Hannington M, Stoffers P, Wright IC, Ditchburn RG, Reyes AG, Baker ET, Massoth GJ, Lupton JE, Walker SL, Greene RR, Soong CWR, Ishibashi J, Lebon GT, Bray CJ, Resing JA (2005) Evolution of a submarine magmatic-hydrothermal system: Brothers volcano, southern Kermadec arc, New Zealand. Econ Geol 100:1097–1133

de Ronde CEJ, Massoth GJ, Butterfield DA, Christenson BW, Ishibashi J, Ditchburn RG, Hannington M, Brathwaite RL, Lupton JE, Kamenetsky VS, Graham IJ, Zellmer GF, Dziak RP, Embley RW, Dekov VM, Munnik F, Lahr J, Evans LJ, Takai K (2011) Submarine hydrothermal activity and gold-rich mineralization at Brothers Volcano, Kermadec Arc, New Zealand. Miner Deposita 46:541–584

de Ronde CEJ, Humphris SE, Höfig TW, Reyes AG (2019) Critical role of caldera collapse in the formation of seafloor mineralization: the case of Brothers volcano. Geology 47:762–766

Diehl A, de Ronde CEJ, Bach W (2020) Subcritical phase separation and occurrence of deep-seated brines at the NW Caldera vent field, Brothers volcano: evidence from fluid inclusions in hydrothermal precipitates. Geofluids 2020:1–22

Dimitriadis I, Papazachos C, Panagiotopoulos D, Hatzidimitriou P, Bohnhoff M, Rische M, Meier T (2010) P and S velocity structures of the Santorini-Coloumbo volcanic system (Aegean Sea, Greece) obtained by non-linear inversion of travel times and its tectonic implications. J Volcanol Geoth Res 195:13–30

Drummond SE, Ohmoto H (1985) Chemical evolution and mineral deposition in boiling hydrothermal systems. Econ Geol 80:126–147

Du J, Audétat A (2020) Early sulfide saturation is not detrimental to porphyry Cu-Au formation. Geology 48:519–524

Edmonds M, Mather TA (2017) Volcanic Sulfides and Outgassing. Elements 13:105–110

Falkenberg JJ, Keith M, Haase KM, Bach W, Klemd R, Strauss H, Yeo IA, Rubin KH, Storch B, Anderson MO (2021) Effects of fluid boiling on Au and volatile element enrichment in submarine arc-related hydrothermal systems. Geochim Cosmochim Acta 307:105–132

Fontboté L, Kouzmanov K, Chiaradia M, Pokrovski GS (2017) Sulfide Minerals in Hydrothermal Deposits. Elements 13:97–103

Fouqué F (1879) Santorin et ses éruptions. G. Masson, Paris

Fytikas M, Innocenti F, Manetti P, Peccerillo A, Mazzuoli R, Villari L (1984) Tertiary to Quaternary evolution of volcanism in the Aegean region. Geol Soc Spec Publ 17:687–699

Gammons CH, Williams-Jones AE (1997) Chemical mobility of gold in the porphyry-epithermal environment. Econ Geol 92:45–59

Georgatou A, Chiaradia M, Kouzmanov K (2021) T-P-fO2 conditions of sulfide saturation in magmatic enclaves and their host lavas. Lithos 398:106313

Georgatou A, Chiaradia M, Klaver M (2022) Deep to shallow sulfide saturation at Nisyros active volcano. Geochem Geophys Geosyst 23:e2021GC010161

Grant HL, Hannington M, Hardardóttir V, Fuchs SH, Schumann D (2020) Trace metal distributions in sulfide scales of the seawater-dominated Reykjanes geothermal system: constraints on subseafloor hydrothermal mineralizing processes and metal fluxes. Ore Geol Rev 116:103145

Halbach P, Nakamura K, Wahsner M, Lange J, Sakai H, Käselitz L, Hansen R-D, Yamano M, Post J, Prause B, Seifert R, Michaelis W, Teichmann F, Kinoshita M, Märten A, Ishibashi J, Czerwinski S, Blum N (1989) Probable modern analogue of Kuroko-type massive sulphide deposits in the Okinawa Trough back-arc basin. Nature 338:496–499

Hannington M (2014) Volcanogenic massive sulfide deposits. In: Treatise on geochemistry. Elsevier 463–488

Hannington M, Scott SD (1989) Gold mineralization in volcanogenic massive sulfides: implications of data from active hydrothermal vents on the modern sea floor. In: Keays RR, Ramsay WRH, Groves DI (eds) The geology of gold deposits: the perspectives in 1988. Society of Economic Geologists, pp 491–507

Hannington M, de Ronde CEJ, Petersen S (2005) Sea-floor tectonics and submarine hydrothermal systems. In: Hedenquist J, Thompson JFH, Goldfarb RJ, Richards JP (eds) One hundredth anniversary volume Society of Economic Geologists

Haraguchi S, Ishizuka H, Ishii T, Fujioka K, Yuasa M, Shibasaki H (2014) Low- and high-temperature alterations of volcanic rocks in the northwestern Philippine Sea, and association with volcanic settings. Island Arc 23:324–343

Hattori K, Takahashi Y, Guillot S, Johanson B (2005) Occurrence of arsenic (V) in forearc mantle serpentinites based on X-ray absorption spectroscopy study. Geochim Cosmochim Acta 69:5585–5596

Hedenquist JW, Lowenstern JB (1994) The role of magmas in the formation of hydrothermal ore deposits. Nature 370:519–527

Heinrich CA (2007) Fluid-fluid interactions in magmatic-hydrothermal ore formation. Rev Mineral Geochem 65:363–387

Heinrich CA, Günther D, Audétat A, Ulrich T, Frischknecht R (1999) Metal fractionation between magmatic brine and vapor, determined by microanalysis of fluid inclusions. Geology 27:755

Holzheid A (2010) Separation of sulfide melt droplets in sulfur saturated silicate liquids. Chem Geol 274:127–135

Hooft EE, Nomikou P, Toomey DR, Lampridou D, Getz C, Christopoulou M-E, O'Hara D, Arnoux GM, Bodmer M, Gray M, Heath BA, VanderBeek BP (2017) Backarc tectonism, volcanism, and mass wasting shape seafloor morphology in the Santorini-Christiana-Amorgos region of the Hellenic Volcanic Arc. Tectonophysics 712:396–414

Huang X-W, Sappin A-A, Boutroy É, Beaudoin G, Makvandi S (2019) Trace element composition of igneous and hydrothermal magnetite from porphyry deposits: relationship to deposit subtypes and magmatic affinity. Econ Geol 114:917–952

Hübscher C, Ruhnau M, Nomikou P (2015) Volcano-tectonic evolution of the polygenetic Kolumbo submarine volcano/Santorini (Aegean Sea). J Volcanol Geoth Res 291:101–111

Jenner FE, St. O'Neill HC, Arculus RJ, Mavrogenes JA (2010) The magnetite crisis in the evolution of arc-related magmas and the initial concentration of Au, Ag and Cu. J Petrol 51:2445–2464

Jenner FE, Arculus RJ, Mavrogenes JA, Dyriw NJ, Nebel O, Hauri EH (2012) Chalcophile element systematics in volcanic glasses from the northwestern Lau Basin. Geochem Geophys Geosyst 13(6)

Jenner FE, Hauri EH, Bullock ES, König S, Arculus RJ, Mavrogenes JA, Mikkelson N, Goddard C (2015) The competing effects of sulfide saturation versus degassing on the behavior of the chalcophile elements during the differentiation of hydrous melts. Geochem Geophys Geosyst 16:1490–1507

Jugo PJ (2009) Sulfur content at sulfide saturation in oxidized magmas. Geology 37:415–418

Keith M, Haase KM, Klemd R, Smith DJ, Schwarz-Schampera U, Bach W (2018) Constraints on the source of Cu in a submarine magmatic-hydrothermal system, Brothers volcano Kermadec island arc. Contrib Mineral Petrol 173(1):6

Kilias SP, Nomikou P, Papanikolaou D, Polymenakou PN, Godelitsas A, Argyraki A, Carey S, Gamaletsos P, Mertzimekis TJ, Stathopoulou E, Goettlicher J, Steininger R, Betzelou K, Livanos I, Christakis C, Bell KC, Scoullos M (2013) New insights into hydrothermal vent processes in the unique shallow-submarine arc-volcano, Kolumbo (Santorini). Greece Sci Rep 3:2421

Klaver M, Carey S, Nomikou P, Smet I, Godelitsas A, Vroon P (2016) A distinct source and differentiation history for Kolumbo submarine volcano, Santorini volcanic field, Aegean arc. Geochem Geophys Geosyst 17:3254–3273

Konstantinou KI (2020) Magma chamber evolution during the 1650 AD Kolumbo eruption provides clues about past and future volcanic activity. Sci Rep 10:15423

Large RR (1992) Australian volcanic-hosted massive sulfide deposits; features, styles, and genetic models. Econ Geol 87:471–510

Lee HJ, Hun Seo J, de Ronde CE, Heinrich CA (2023) Fluid inclusion evidence for subseafloor magmatic-hydrothermal processes at Brothers volcano, Kermadec arc, New Zealand. Econ Geol 118:1741–1760

Li Y, Audétat A (2012) Partitioning of V, Mn Co, Ni, Cu, Zn, As, Mo, Ag, Sn, Sb, W, Au, Pb, and Bi between sulfide phases and hydrous basanite melt at upper mantle conditions. Earth Planet Sci Lett 355:327–340

Lilley MD, Butterfield DA, Lupton JE, Olson EJ (2003) Magmatic events can produce rapid changes in hydrothermal vent chemistry. Nature 422:878–881

Lowenstern J (2001) Carbon dioxide in magmas and implications for hydrothermal systems. Miner Deposita 36:490–502

Martin AJ, Jamieson JW, de Ronde CEJ, Humphris SE, McDonald I, Layne GD, Piercey G, MacLeod CJ (2023) Trace metal and sulfur cycling in a hydrothermally active arc volcano: deep-sea drilling of the Brothers volcano, Kermadec arc, New Zealand. Miner Deposita 58:403–425

Mavrogenes JA, O'Neill HS (1999) The relative effects of pressure, temperature and oxygen fugacity on the solubility of sulfide in mafic magmas. Geochim Cosmochim Acta 63:1173–1180

McVey BG, Hooft E, Heath BA, Toomey DR, Paulatto M, Morgan JV, Nomikou P, Papazachos CB (2020) Magma accumulation beneath Santorini volcano, Greece, from P-wave tomography. Geology 48:231–235

Mungall JE, Brenan JM, Godel B, Barnes SJ, Gaillard F (2015) Transport of metals and sulphur in magmas by flotation of sulphide melt on vapour bubbles. Nature Geosci 8:216–219

Nadeau O, Mick E, Robidoux P, Grassa F, Brusca L, Voinot A, Leybourne MI (2021) Lithium isotopes and Cu-Au concentrations in hydrothermal alterations from Solfatara Volcano, Campi Flegrei caldera complex, and La Fossa volcano, Vulcano Island, Italy: insights into epithermal ore forming environments. Ore Geol Rev 130:103934

Nadoll P, Angerer T, Mauk JL, French D, Walshe J (2014) The chemistry of hydrothermal magnetite: a review. Ore Geol Rev 61:1–32

Nomikou P, Carey S, Papanikolaou D, Croff Bell K, Sakellariou D, Alexandri M, Bejelou K (2012) Submarine volcanoes of the Kolumbo volcanic zone NE of Santorini Caldera, Greece. Global Planet Change 90:135–151

Nomikou P, Carey S, Croff Bell KL, Papanikolaou D, Bejelou K, Alexandri M, Cantner K, Martin JF (2013) Morphological analysis and related volcanic features of the Kolumbo submarine volcanic chain (NE of Santorini Island, Aegean Volcanic Arc). Zeitschrift für Geomorphologie 57:29–47

Nomikou P, Druitt TH, Hübscher C, Mather TA, Paulatto M, Kalnins LM, Kelfoun K, Papanikolaou D, Bejelou K, Lampridou D, Pyle DM, Carey S, Watts AB, Weiß B, Parks MM (2016) Post-eruptive flooding of Santorini caldera and implications for tsunami generation. Nat Commun 7:13332

Nomikou P, Hübscher C, Carey S (2019) The Christiana–Santorini–Kolumbo volcanic field. Elements 15:171–176

Nomikou P, Polymenakou PN, Rizzo AL, Petersen S, Hannington M, Kilias SP, Papanikolaou D, Escartin J, Karantzalos K, Mertzimekis TJ, Antoniou V, Krokos M, Grammatikopoulos L, Italiano F, Caruso CG, Lazzaro G, Longo M, Sciré Scappuzzo S, D'Alessandro W, Grassa F, Bejelou K, Lampridou D, Katsigera A, Dura A (2022) SANTORY: SANTORini's seafloor volcanic ObservatorY. Front Mar Sci 9:796376

Papanikolaou D (2013) Tectonostratigraphic models of the Alpine terranes and subduction history of the Hellenides. Tectonophysics 595:1–24

Park J-W, Campbell IH, Kim J, Moon J-W (2015) The role of late sulfide saturation in the formation of a Cu- and Au-rich magma: insights from the platinum group element geochemistry of Niuatahi-Motutahi lavas, Tonga rear arc. J Petrol 56:59–81

Paton C, Hellstrom J, Paul B, Woodhead J, Hergt J (2011) Iolite: freeware for the visualisation and processing of mass spectrometric data. J Anal at Spectrom 26:2508

Patten CGC, Barnes S-J, Mathez EA, Jenner FE (2013) Partition coefficients of chalcophile elements between sulfide and silicate melts and the early crystallization history of sulfide liquid: LA-ICP-MS analysis of MORB sulfide droplets. Chem Geol 358:170–188

Patten CGC, Pitcairn IK, Teagle DAH, Harris M (2016) Mobility of Au and related elements during the hydrothermal alteration of the oceanic crust: implications for the sources of metals in VMS deposits. Miner Deposita 51:179–200

Patten CGC, Pitcairn IK, Teagle D (2017) Hydrothermal mobilisation of Au and other metals in supra-subduction oceanic crust: insights from the Troodos ophiolite. Ore Geol Rev 86:487–508

Patten CGC, Pitcairn IK, Alt JC, Zack T, Lahaye Y, Teagle DAH, Markdahl K (2020) Metal fluxes during magmatic degassing in the oceanic crust: sulfide mineralisation at ODP site 786B, Izu-Bonin forearc. Miner Deposita 55:469–489

Patten CGC, Beranoaguirre A, Hector S, Gudelius D, Kolb J, Eiche E (2023) Improved whole rock low detection limit gold analysis by LA-ICP-MS utilizing pressed-powder-pellets. Int J Mass Spectrom 488:117039

Patten CGC, Hector S, Kilias SP, Ulrich M, Peillod A, Beranoaguirre A, Nomikou P, Eiche E, Kolb J (2024) Transfer of sulfur and chalcophile metals via sulfide-volatile compound drops in the Christiana-Santorini-Kolumbo volcanic field. Nat Commun (in press)

Preine J, Karstens J, Hübscher C, Nomikou P, Schmid F, Crutchley GJ, Druitt TH, Papanikolaou D (2022) Spatio-temporal evolution of the Christiana-Santorini-Kolumbo volcanic field, Aegean Sea. Geology 50:96–100

Richard F (1657) Relation de ce qui s'est passé de plus remarquable à Sant-Erini, isle de l'Archipel, depuis l'établissement des Pères de la Compagnie de Jésus en icelle. S. Cramoisy, Paris

Richards JP (2011) Magmatic to hydrothermal metal fluxes in convergent and collided margins. Ore Geol Rev 40:1–26

Richards JP (2015) The oxidation state, and sulfur and Cu contents of arc magmas: implications for metallogeny. Lithos 233:27–45

Rizzo AL, Caracausi A, Chavagnac V, Nomikou P, Polymenakou PN, Mandalakis M, Kotoulas G, Magoulas A, Castillo A, Lampridou D (2016) Kolumbo submarine volcano (Greece): an active window into the Aegean subduction system. Sci Rep 6:28013

Rizzo AL, Caracausi A, Chavagnac V, Nomikou P, Polymenakou PN, Mandalakis M, Kotoulas G, Magoulas A, Castillo A, Lampridou D, Marusczak N, Sonke JE (2019) Geochemistry of CO2-rich gases venting from submarine volcanism: the case of Kolumbo (Hellenic Volcanic Arc, Greece). Front Earth Sci 7:60

Rouwet D, Hidalgo S, Joseph EP, González-Ilama G (2019) Fluid geochemistry and volcanic unrest: dissolving the haze in time and space. In: Gottsmann J, Neuberg J, Scheu B (eds) Volcanic unrest. Springer International Publishing, Cham, pp 221–239

Schmid F, Petersen G, Hooft E, Paulatto M, Chrapkiewicz K, Hensch M, Dahm T (2022) Heralds of future volcanism: swarms of microseismicity beneath the submarine Kolumbo volcano indicate opening of near-vertical fractures exploited by ascending melts. Geochem Geophys Geosyst 23:e2022GC010420

Shikazono N (2003) Geochemical and tectonic evolution of arc-backarc hydrothermal systems: implication for origin of Kuroko and epithermal vein-type mineralizations and the global geochemical cycle, 1st ed. Developments in geochemistry, vol 8. Elsevier, Amsterdam, Boston

Shu Y, Nielsen SG, Le Roux V, Wörner G, Blusztajn J, Auro M (2022) Sources of dehydration fluids underneath the Kamchatka arc. Nat Commun 13:4467

Sigurdsson H, Carey S, Alexandri M, Vougioukalakis G, Croff K, Roman C, Sakellariou D, Anagnostou C (2006) Marine investigations of Greece's Santorini volcanic field. Eos Trans Am Geophys Union 87:337–342

Sillitoe RH (2010) Porphyry copper systems. Econ Geol 105:3–41

Skirrow RG, Franklin JM (1994) Silicification and metal leaching in semiconformable alteration beneath the Chisel Lake massive sulfide deposit, Snow Lake, Manitoba. Econ Geol 89:31–50

Smythe DJ, Wood BJ, Kiseeva ES (2017) The S content of silicate melts at sulfide saturation: new experiments and a model incorporating the effects of sulfide composition. Am Miner 102:795–803

Spandler C, O'Neill HS (2010) Diffusion and partition coefficients of minor and trace elements in San Carlos olivine at 1,300°C with some geochemical implications. Contrib Mineral Petrol 159:791–818

Stanton RL (1994) Ore elements in arc lavas. Oxford science publications. Clarendon Press; Oxford University Press, Oxford, New York

Sun W, Arculus RJ, Kamenetsky VS, Binns RA (2004) Release of gold-bearing fluids in convergent margin magmas prompted by magnetite crystallization. Nature 431:975–978

Thal J, Tivey M, Yoerger DR, Bach W (2016) Subaqueous cryptodome eruption, hydrothermal activity and related seafloor morphologies on the andesitic North Su volcano. J Volcanol Geoth Res 323:80–96

Wang Z, Park J-W, Wang X, Zou Z, Kim J, Zhang P, Li M (2019) Evolution of copper isotopes in arc systems: insights from lavas and molten sulfur in Niuatahi volcano, Tonga rear arc. Geochim Cosmochim Acta 250:18–33

Williams-Jones AE, Bowell RJ, Migdisov AA (2009) Gold in Solution. Elements 5:281–287

Yao Z, Mungall JE (2020) Flotation mechanism of sulphide melt on vapour bubbles in partially molten magmatic systems. Earth Planet Sci Lett 542:116298

Yeats CJ, Parr JM, Binns RA, Gemmell JB, Scott SD (2014) The SuSu Knolls hydrothermal field, eastern Manus basin, Papua New Guinea: an active submarine high-sulfidation copper-gold system. Econ Geol 109:2207–2226

Zegkinoglou NN, Mathur R, Kilias SP, Godfrey L, Pletsas V, Nomikou P, Zaronikola N (2023) Boiling-induced extreme Cu isotope fractionation in sulfide minerals forming by active hydrothermal diffusers at the Aegean Kolumbo volcano: evidence from in situ isotope analysis. Geology 51:1072–1076

Publisher's Note Springer Nature remains neutral with regard to jurisdictional claims in published maps and institutional affiliations.